2024 GSS Flash Talks 2 (8/1/24)
Zeno Tecchiolli
Kassia Schraufnagel
Veronika C Bayer
Keely Willis
Alex Wiedman
Hengqian Liu
Dylan Schmeling
Michael Czekanski
Shibangi Majumder
John Kappel
Daniel Alexander Klasing
Francisco Javier Escoto López
Sophia Gray Arnold
Issra Ali

PPPL Flash Talks

PPPL/Simons Foundation graduate summer school

July 29- August 2, 2024

Zeno Tecchiolli

1st year PhD at EPFL (Lausanne, Switzerland) and Swiss Plasma Center

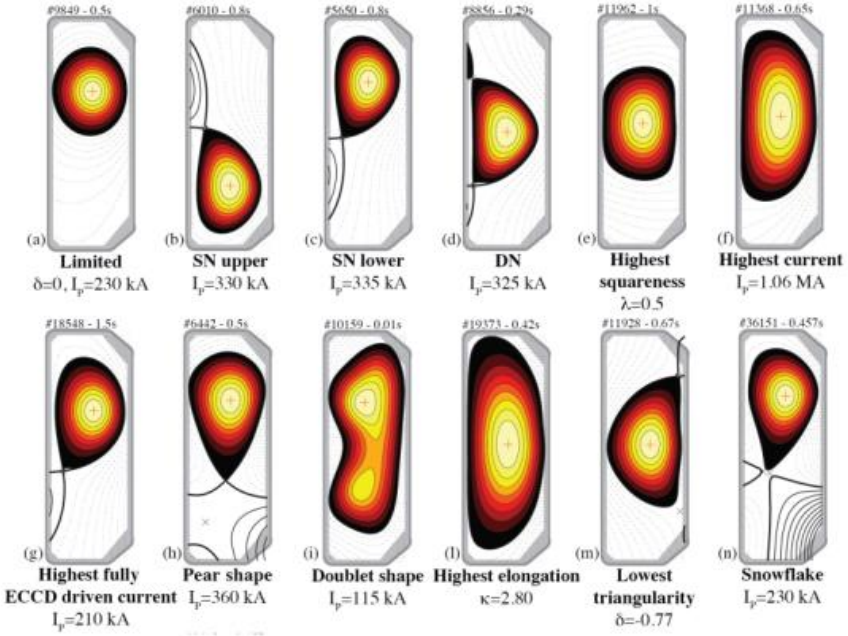

Fundamental characterization of plasma turbulence in the edge of stellarators
Optimization of heat loads and turbulent flux in stellarators

Work with Prof Paolo Ricci and Dr. Joaquim Loizu, using the drift-reduced Braginskii equations solved by the GBS code*

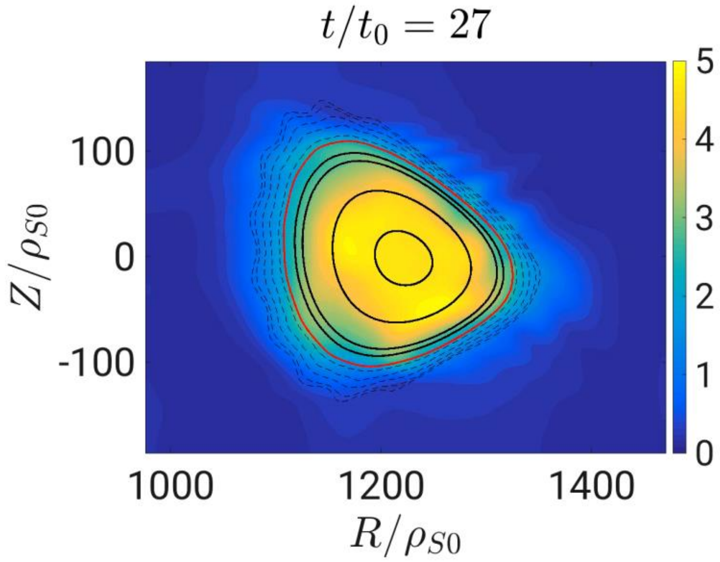

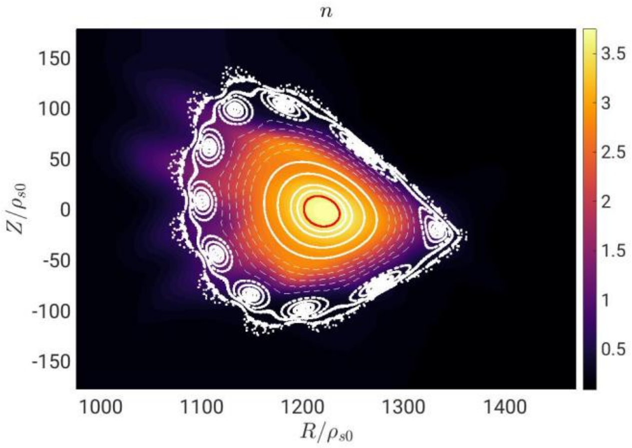

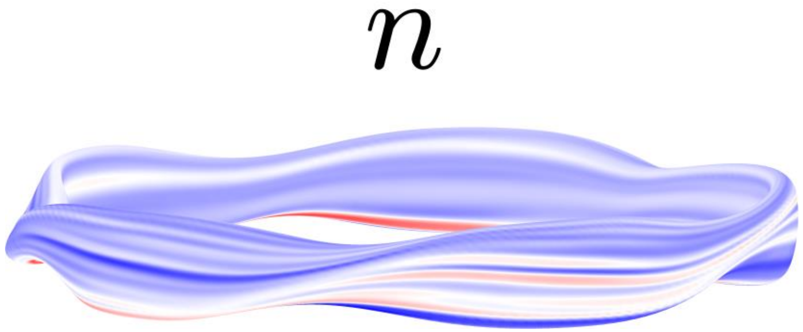

*M. Giacomin, et al. *Journal of Computational Physics* 463 (2022): 111294

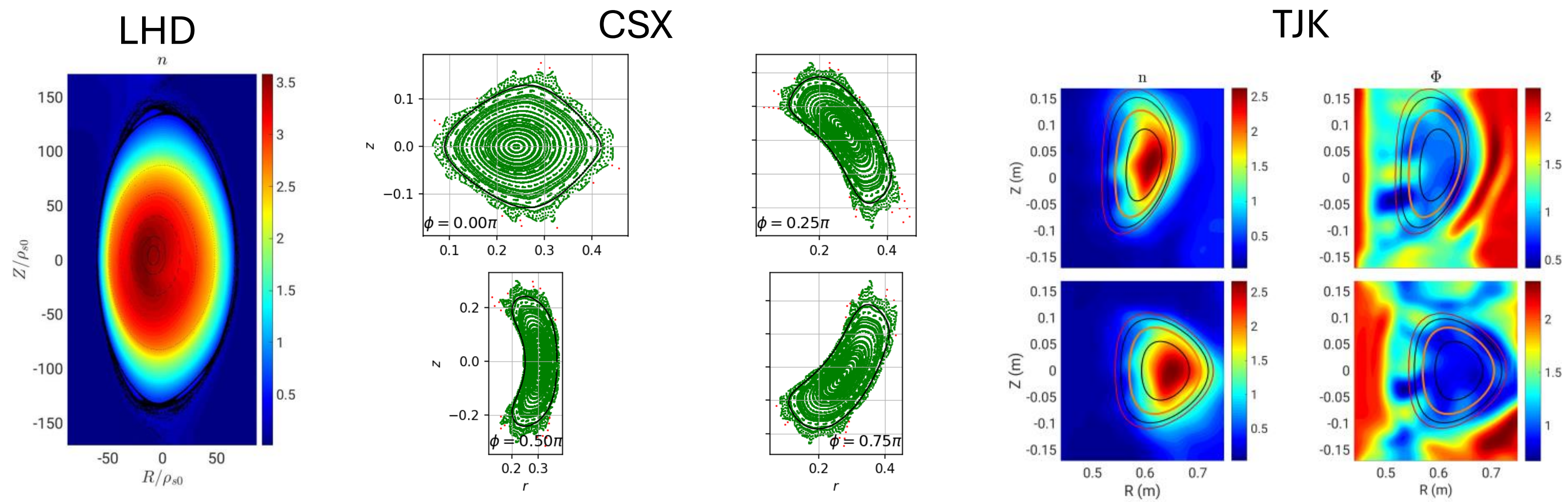

Collaboration with LHD, TJK, HSX, CSX

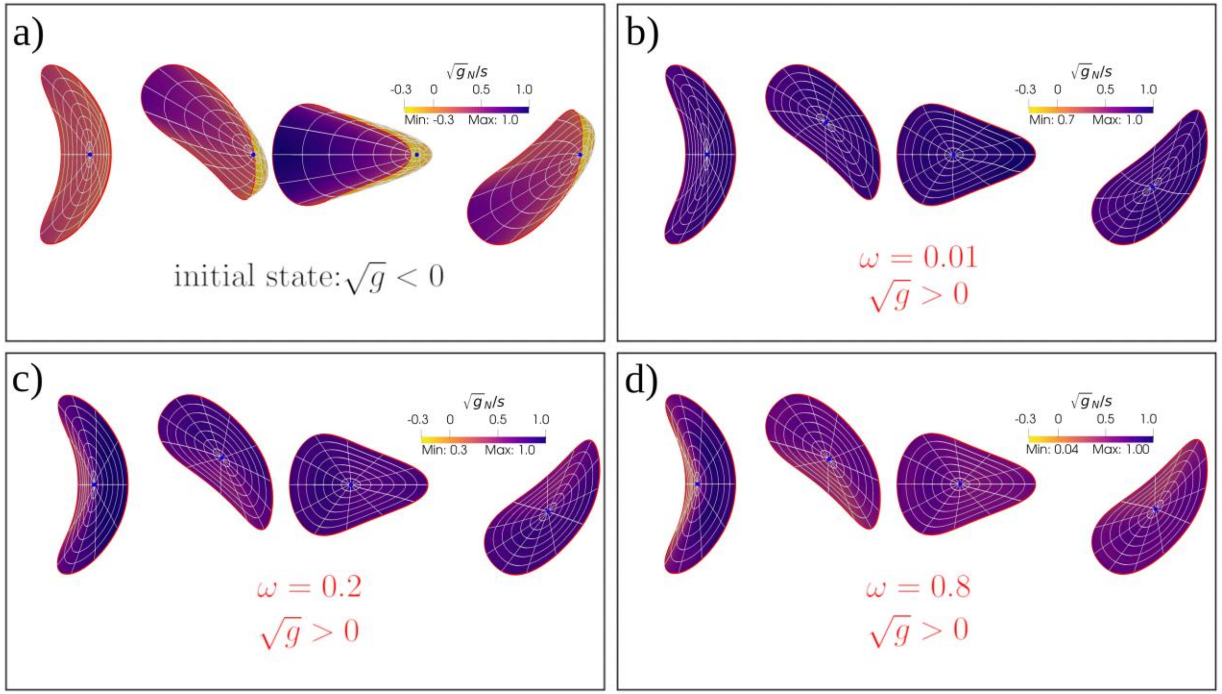

Constructing coordiates for arbitrarily shaped toroidal domain*

Collaboration with Stuart Hudston (PPPL) and Florian Hinderlang (IPP - Garching)

*Z.Tecchiolli et al, arxiv https://arxiv.org/abs/2405.08173

APEX Collaboration: a brief overview

Veronika C Bayer

APEX Collaboration

Step 1:
Obtain positrons from world-class source (up to 10^9/s)

Step 2:
Use a series of non-neutral plasma traps to collect positrons, until we have enough to make a plasma.

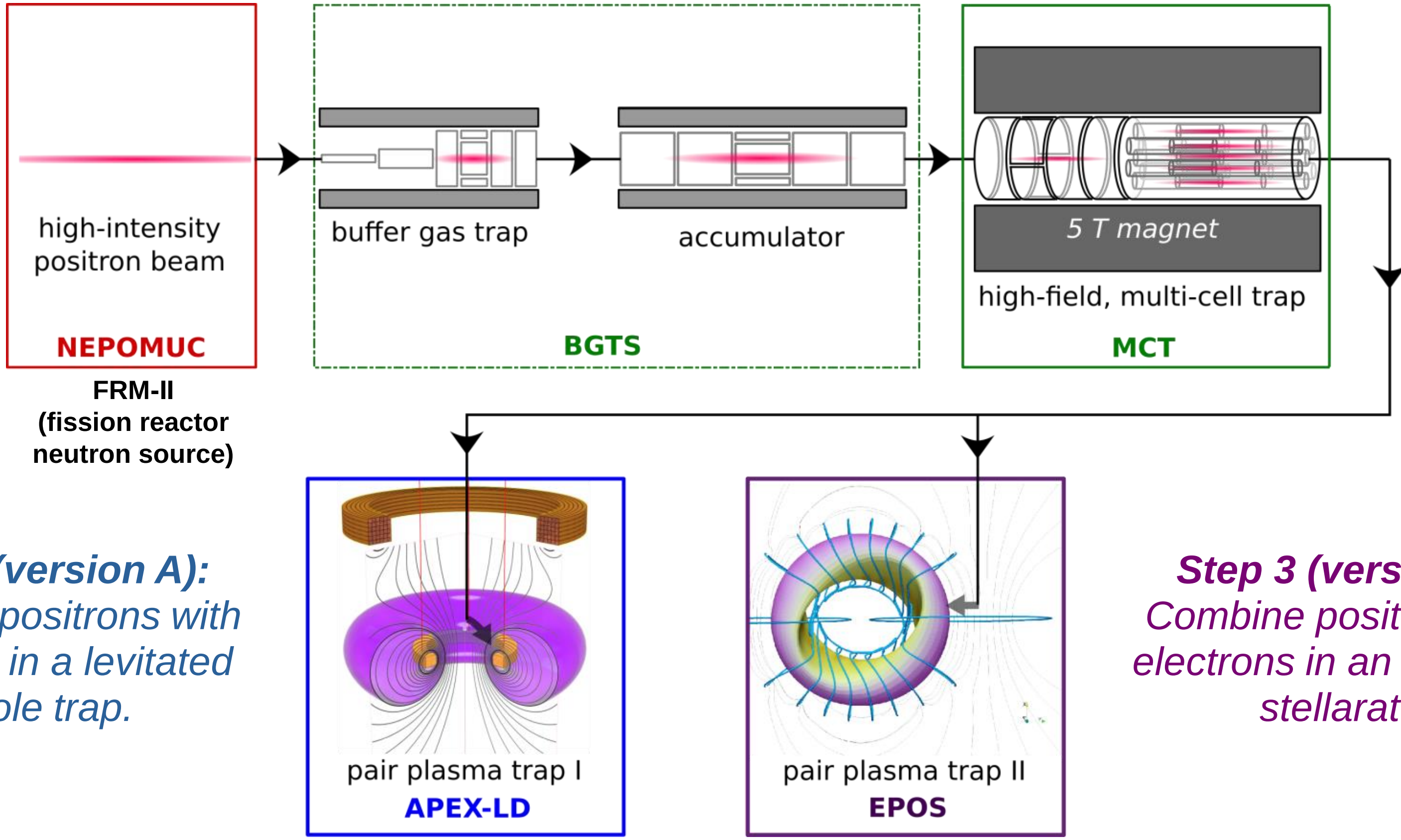

Step 3 (version A):
Combine positrons with electrons in a levitated dipole trap.

Step 3 (version B):
Combine positrons with electrons in an optimized stellarator.

Step 4: *Study the collective, quasineutral behavior of our pair plasmas*

Stoneking, *et al.* (2020) *J. Plasma Phys.* **86**, 155860601

APEX-LD

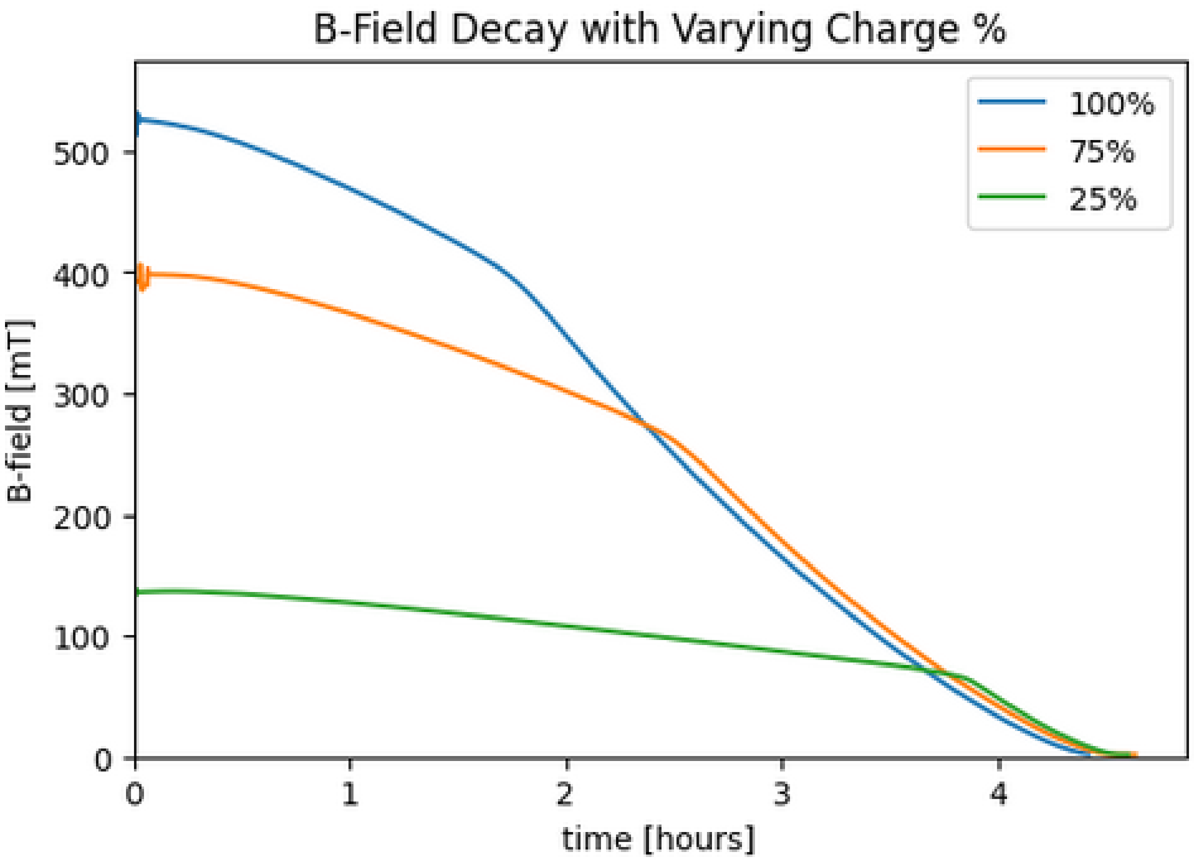
B-Field Decay with Varying Charge %
100%
75%
25%
B-field [mT]
500
400
300
200
100
0
0
1
2
3
4
time [hours]

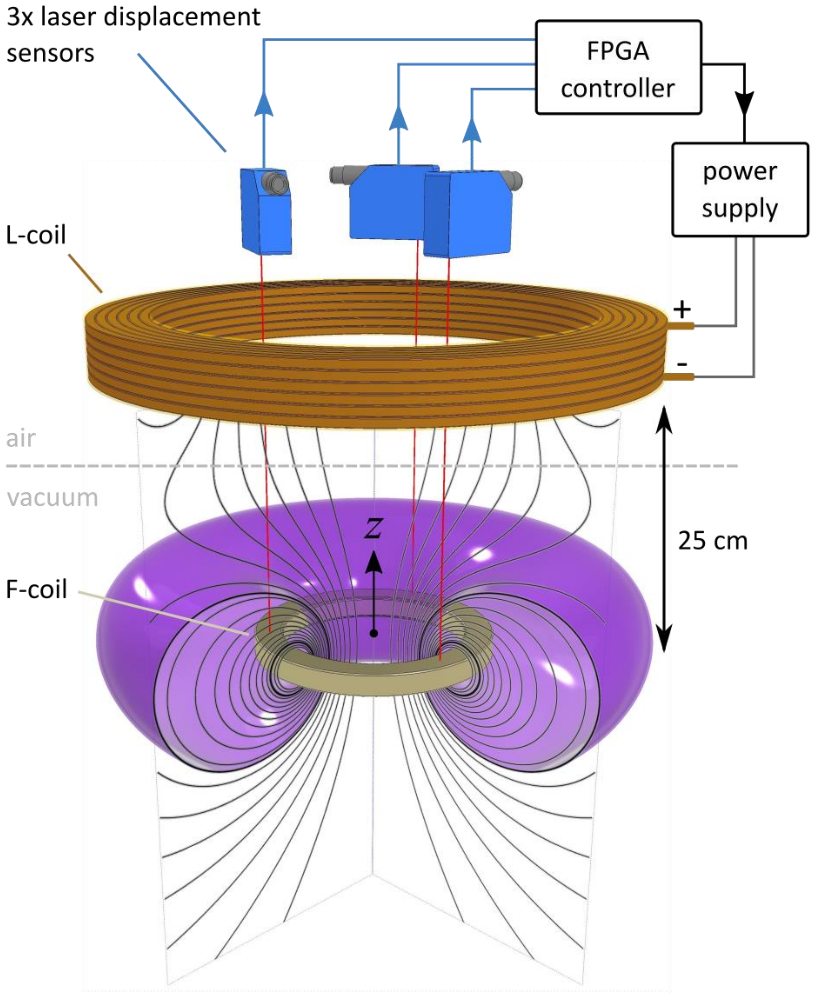
3x laser displacement sensors
FPGA controller
power supply
L-coil
+
-
air
vacuum
z
25 cm
F-coil

APEX-LD

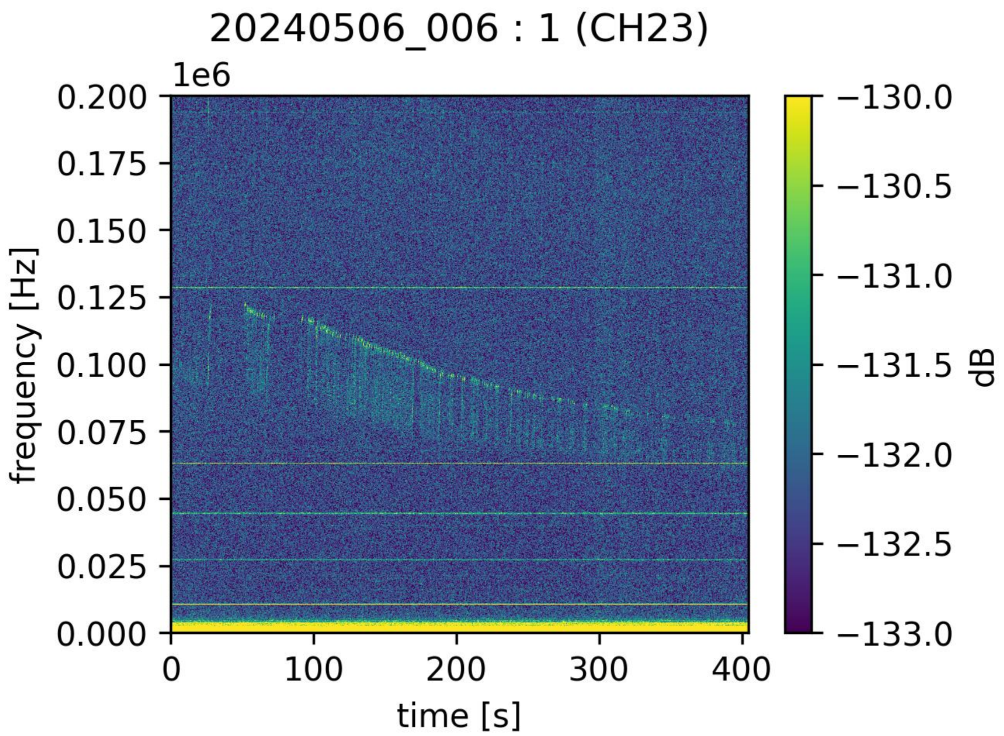

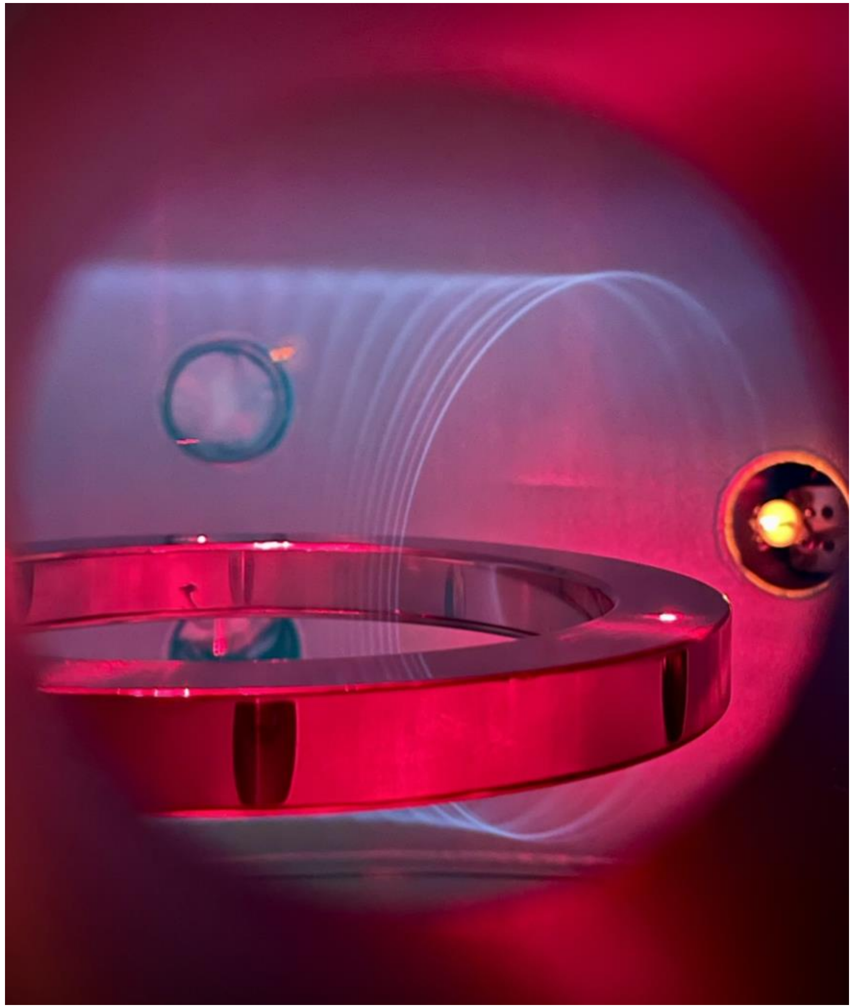

PhD Goals:

a) Understand and *generate e- plasma* in APEX-LD

b) Use E x B drift to *inject positron pulses* into an e-plasma

c) *Diagnose e-e+ plasmas* in various traps

Thanks for listening

EPOS

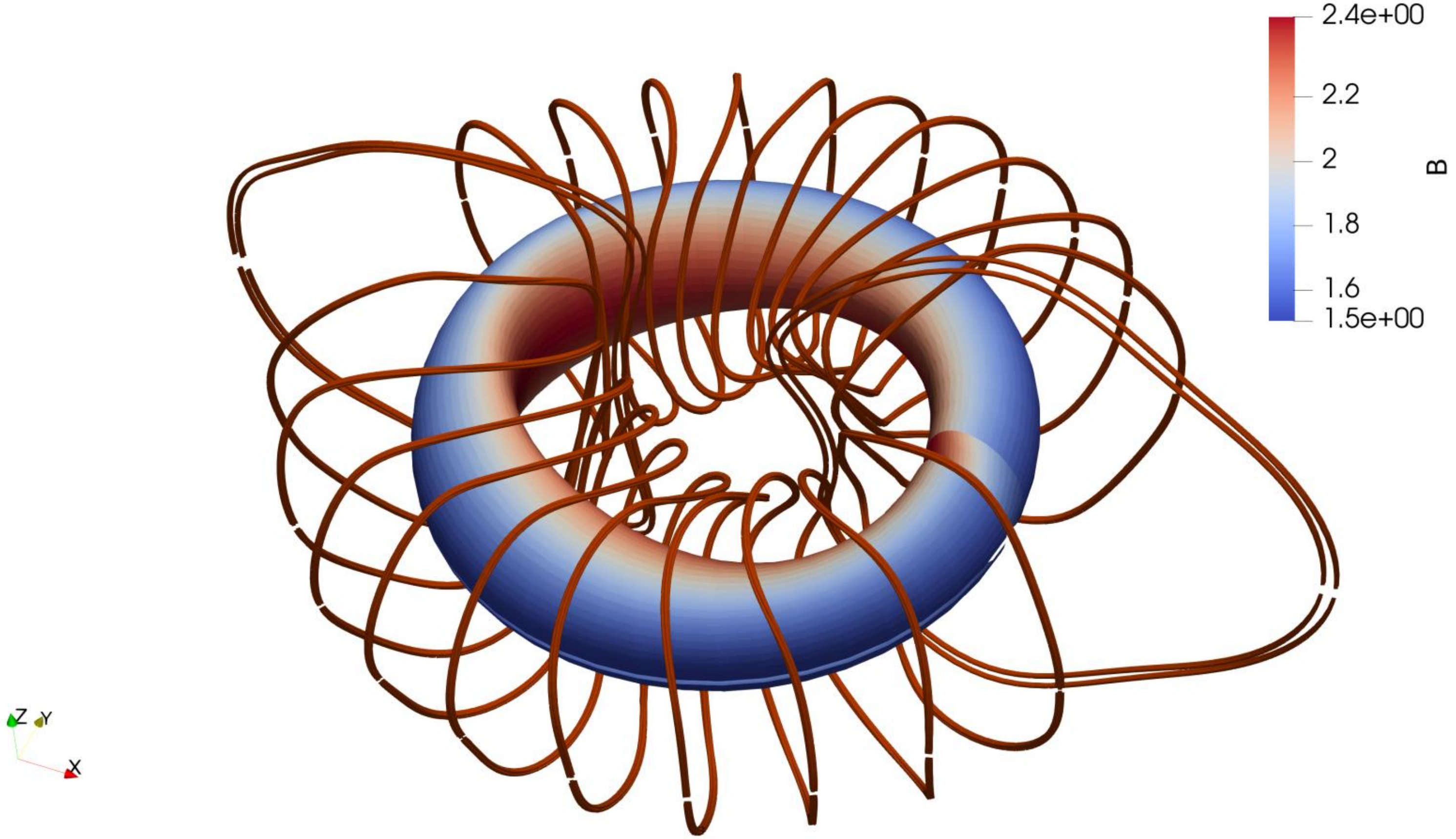

Princeton Plasma Physics Laboratory / Simons Foundation Graduate Summer School

My Self-Introduction and Recent Work

2024.08.01

HengQian Liu
珩骞 刘

About Me

First-year graduate student

- **My name**

  HengQian Liu （珩骞 刘）

- **From School**

  University of Science and Technology of China， USTC

- **My Advisor is**

  Prof. CaoXiang Zhu

- **Study in**

  Nuclear Science and Technology

  - **Undergraduate** ： Fission Engineering
  - **Graduate** ： Plasma Physics & Fusion Engineering
    - **Now major in** ： Stellarator Optimize
    - Learned STELLOPT\SIMSOPT\DESC\SPEC\SIMPLE\SFINCS\FOCUS\REGCOIL....

Keen on nuclear science

Not only studying but also popularizing

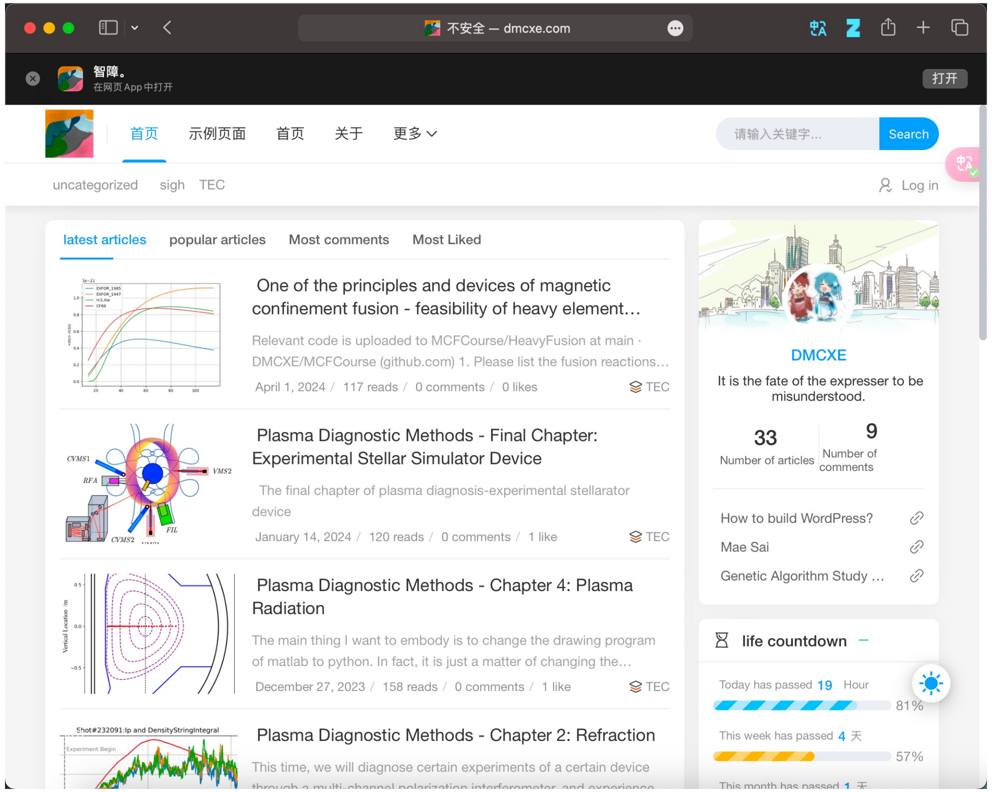

➢ Omnigenity geometric feature[Cary and Shasharina PRL 1996]

- The contours of the magnetic field B are closed toroidally, poloidally of both.
- The contours of Maximum-B are straight.
- $\partial\Delta_\theta/\partial\alpha = 0$ and $\partial\Delta_\zeta/\partial\alpha = 0$: the separations in ζ and θ between the pair of points on opposite branches of a field line but at the same B
- In a magnet line coordinate system, the magnetic field distribution is independent of the magnet line labels

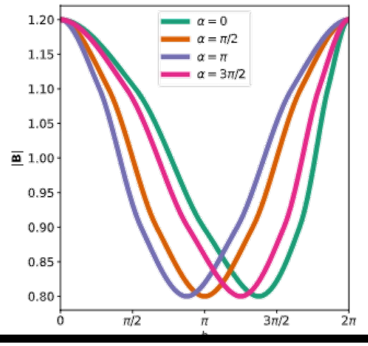

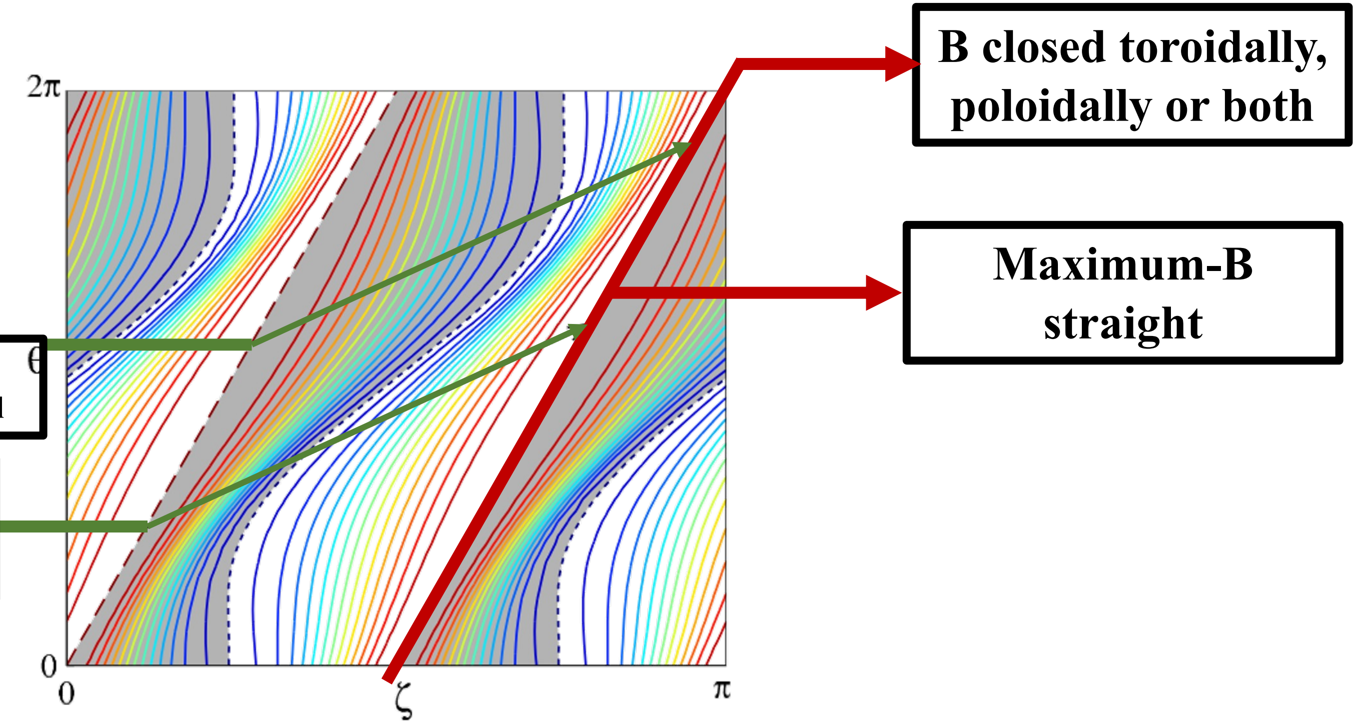

➢**Construct a magnetic field distribution along the magnetic field lines with the same maximum and minimum values**[Cary and Shasharina PRL1996]

$$\boldsymbol{B = B_0(1+\epsilon_r cos(\eta))}$$

➢**Constructing Omnigenous fuction i.e. satisfying the target coordinate transformation** $(\boldsymbol{\eta}, \boldsymbol{\alpha}) \leftrightarrow (\boldsymbol{\zeta_B}, \boldsymbol{\theta_B})$

$$\begin{cases} \zeta = \eta + g(\theta,\eta) \;\; for \;\; 0 \le \eta \le \pi \\ \zeta = 2\pi - \eta + g\left(\theta - \dfrac{\Delta\zeta(\eta)}{q_h}, 2\pi - \eta\right) + \Delta\zeta(\eta) \;\; for \;\; \eta > \pi \\ g(\theta,\eta) = 0 \; when \; \eta(\zeta) = 0, 2\pi \end{cases}$$

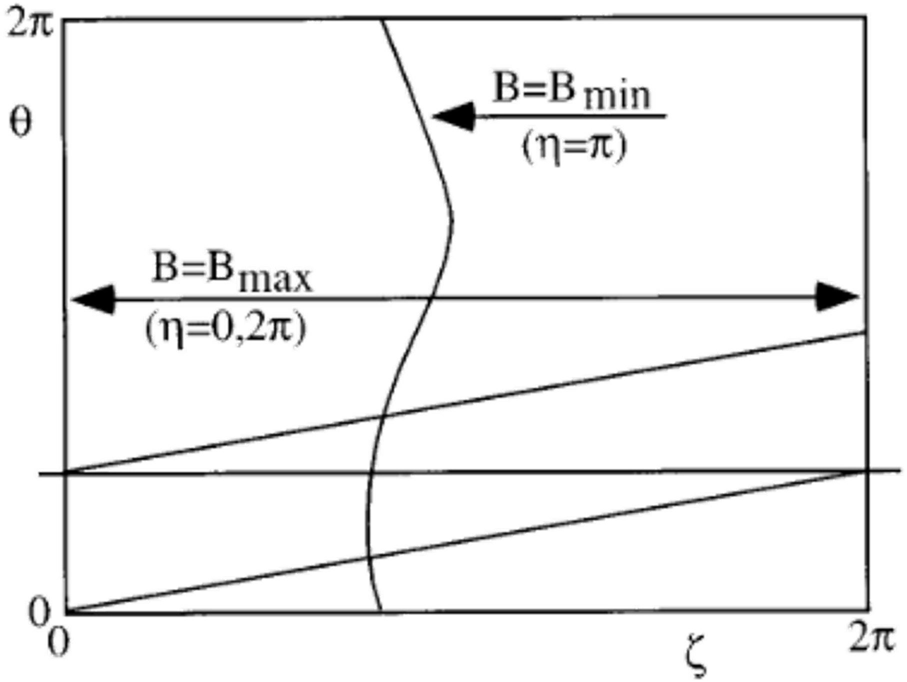

Safety factor q_h:

$$q_h = Nq - 1$$

Rotational transformation ι_h:

$$\iota_h = \frac{\iota}{N - \iota}$$

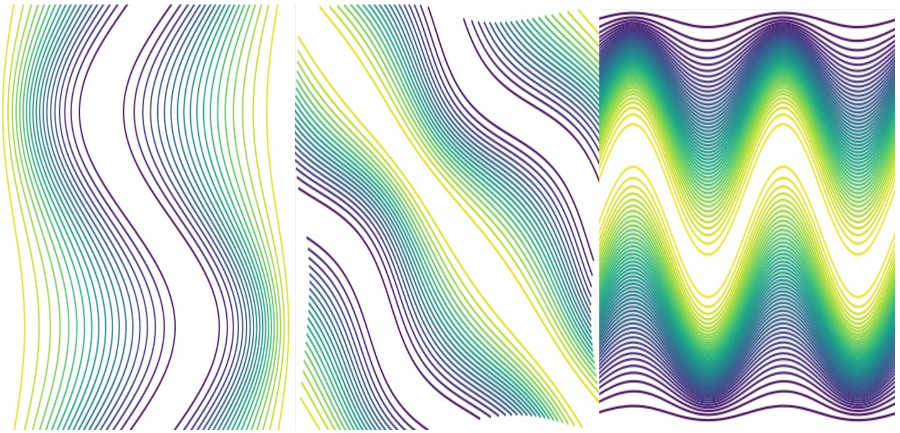

Main Focus
Omnigenity Optimize

➢**C-S Mapping's Coordinate transformation $(\eta,\alpha) \leftrightarrow (\zeta_B,\theta_B)$ not correlate MN**

➢**Landreman Mapping has the form**[Landreman POP 2012]

$$\tilde{\zeta}(\eta,\tilde{\theta}) = \begin{cases} \pi - s\left(\eta,\tilde{\theta}+\tilde{\iota}D(\eta)\right) - D(\eta) & \text{if } 0 \le \eta \le \pi \\ \pi + s\left(2\pi-\eta,-\tilde{\theta}+\tilde{\iota}D(2\pi-\eta)\right) + D(2\pi-\eta) & \text{if } \pi < \eta \le 2\pi \end{cases}$$

- **Dudt Mapping without Radial Interpolation**[Dudt arxiv 2023]

$$h = 2\eta + \pi + \sum_{m=0}^{M_\eta} \sum_{n=-N_\alpha}^{N_\alpha} x_{mn} F_m(\eta) F_{nN_{FP}}(\alpha)$$

  - F characterized as the Fourier coefficient

$$F_k(y) = \begin{cases} \cos(|k|y) & \text{for } k \ge 0 \\ \sin(|k|y) & \text{for } k < 0 \end{cases}$$

➢**Upper wavy line shows that $\tilde{\zeta},\tilde{\theta},\tilde{\iota}$ is in computational space， especially $\tilde{\zeta},\tilde{\theta}$ both in range $[0,2\pi]$， respect to real space as**

- $(M,N)=(1,0)$ i.e. **Toroidal Omnigenity**： $\tilde{\theta}=N_p\zeta, \tilde{\zeta}=\theta, \tilde{\iota}=N_p/\iota$
- $(M,N)=(M,\mathrm{N}=\ non\ \ zero)$ i.e. **Helicity Omnigenity**、**Poloidal Omnigenity**：
$$\tilde{\theta}=\theta, \tilde{\zeta}=(N\zeta-M\theta)N_p, \tilde{\iota}=\iota/[(N-\iota M)N_p]$$

Main Focus

Omnigenity Optimize

➢ **Landreman Mapping has the form**

$$\tilde{\zeta}(\eta,\tilde{\theta}) = \begin{cases} \pi - s\left(\eta, \tilde{\theta} + \tilde{\iota} D(\eta)\right) - D(\eta) & \text{if } 0 \le \eta \le \pi \\ \pi + s\left(2\pi - \eta, -\tilde{\theta} + \tilde{\iota} D(2\pi - \eta)\right) + D(2\pi - \eta) & \text{if } \pi < \eta \le 2\pi \end{cases}$$

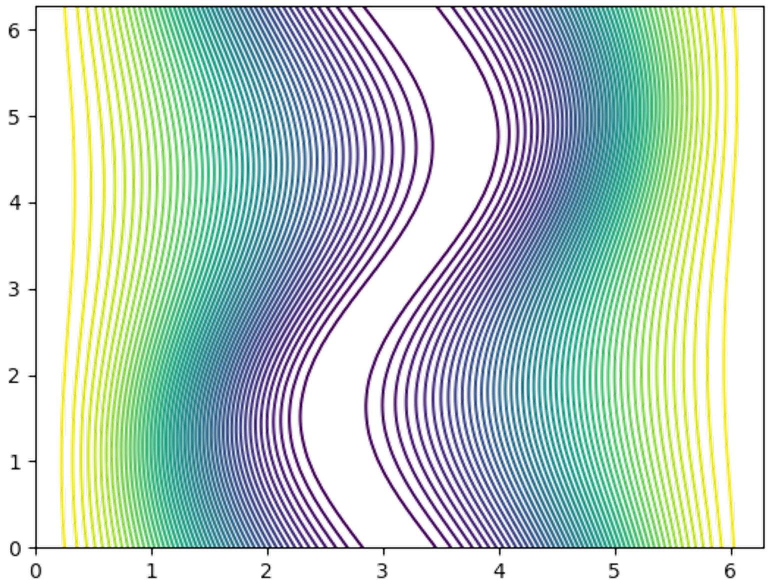

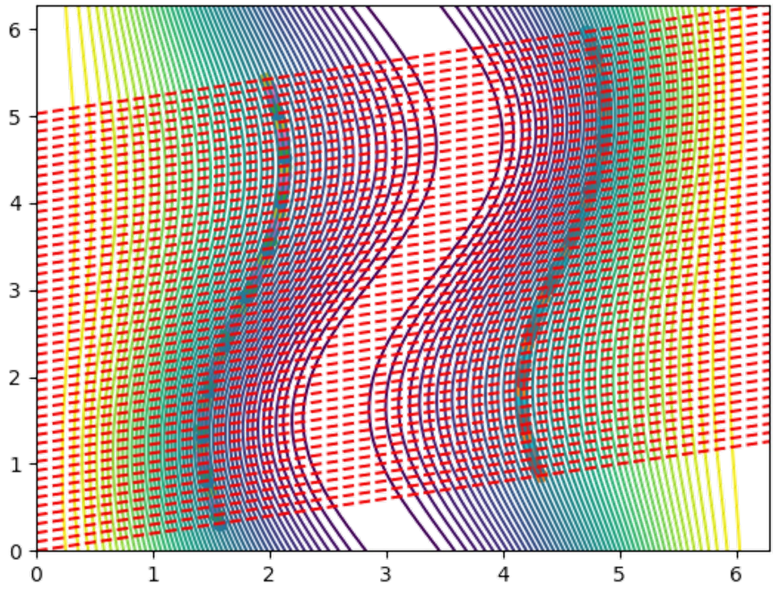

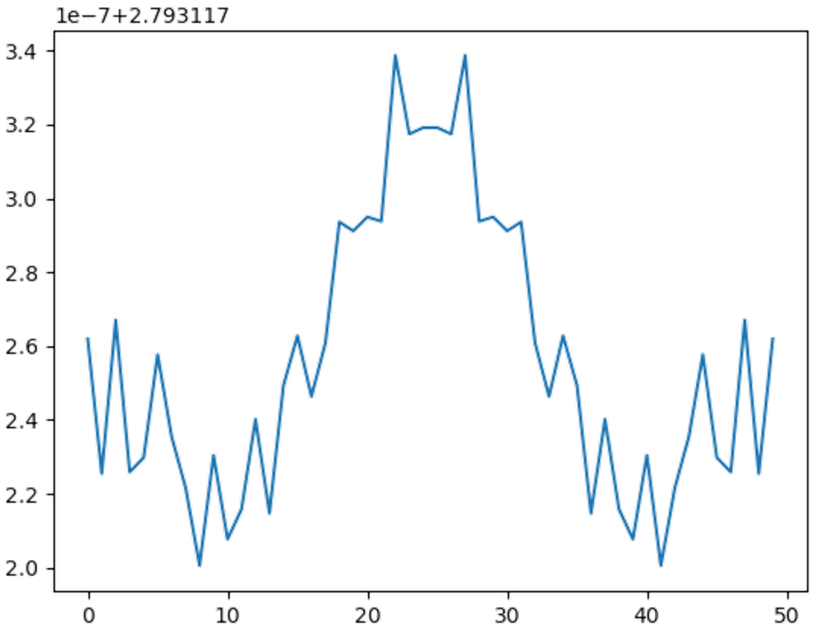

(Hidden Batman)

Omnigenity Example

Poloidal Omnigenity

Nfp = 2 Iota = 0.4 A=6 NO WARMSTART NO alpha particle loss when s=0.25 t=0.2s Landreman-like Mapping

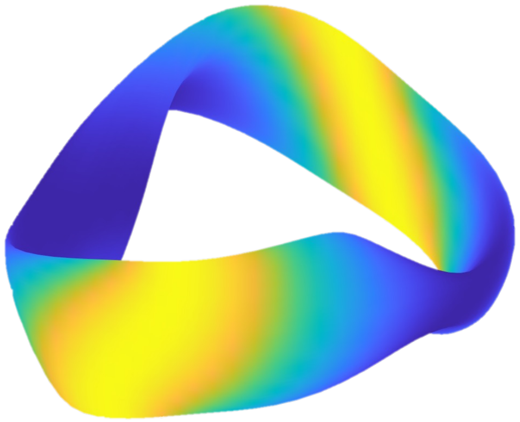

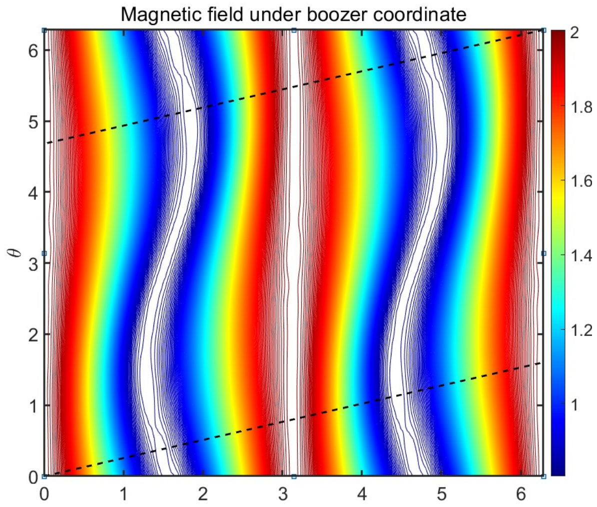

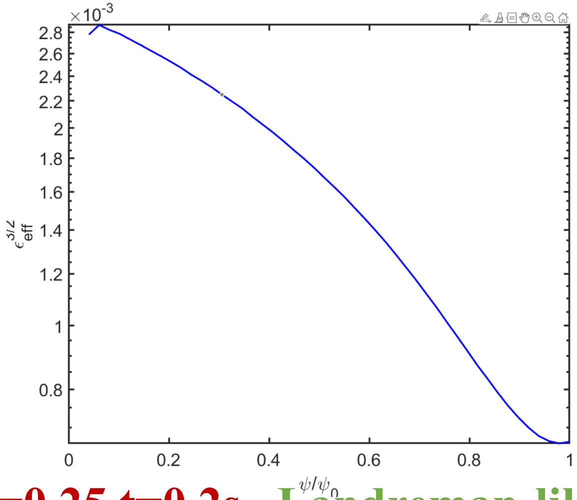

Nfp = 3 Iota = -0.8 A=8 NO WARMSTART NO alpha particle loss when s=0.25 t=0.2s Landreman-like Mapping

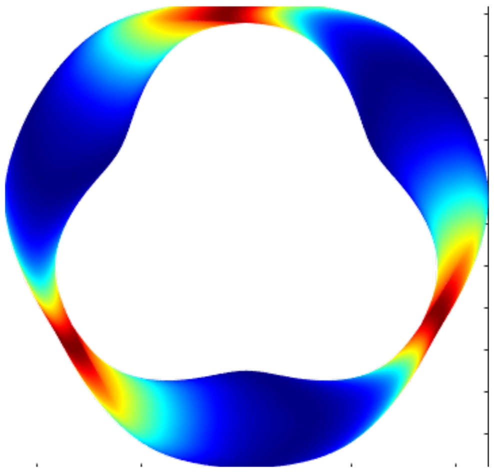

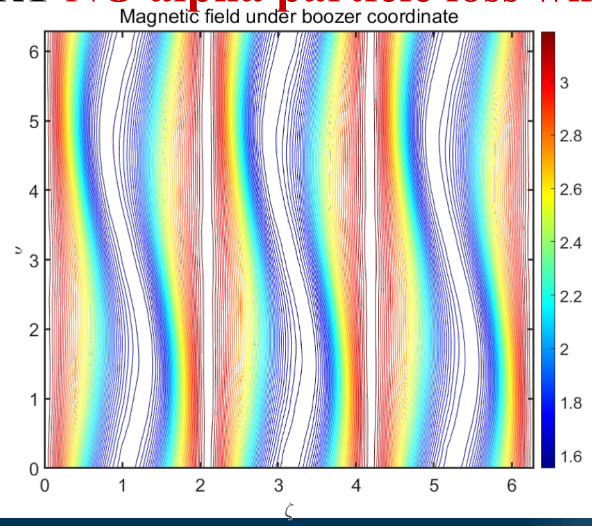

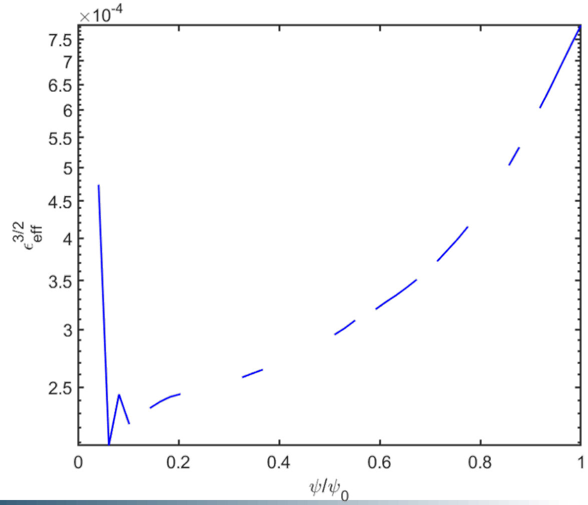

Omnigenity Example

Poloidal Omnigenity

Nfp = 2 Iota = -0.4 A=6 NO WARMSTART With WELL Landreman-like Mapping

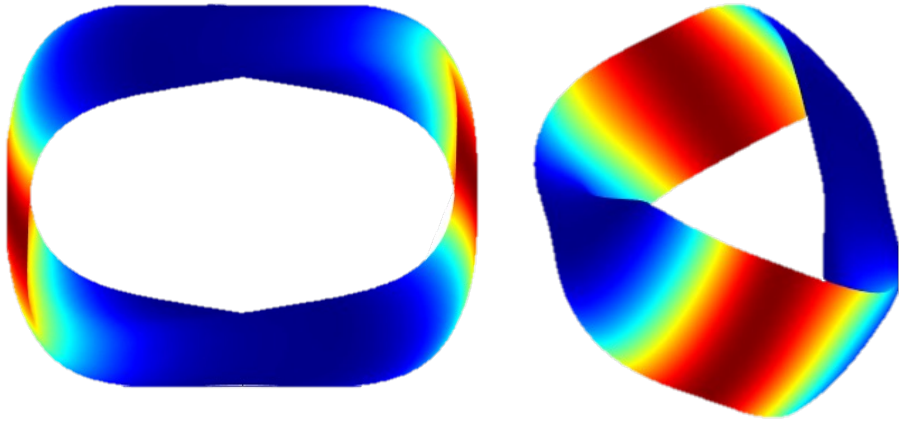

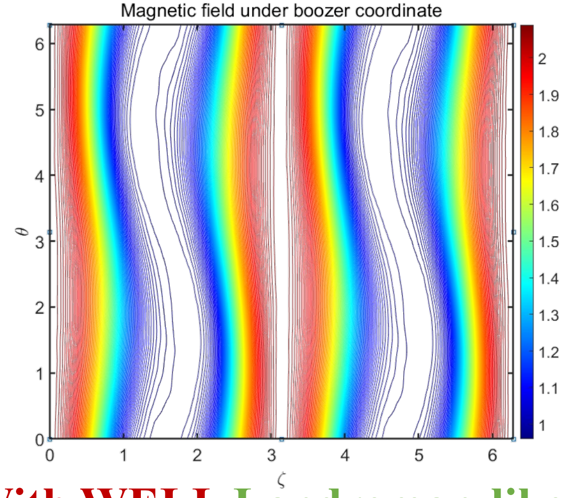

SQUID-like but lack of turbulence optimization

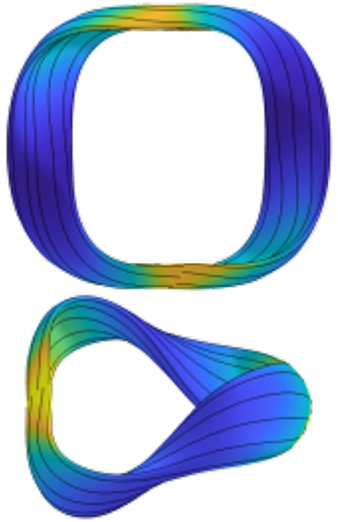

Nfp = 3 Iota = -0.72 A=6 NO WARMSTART With WELL Landreman-like Mapping

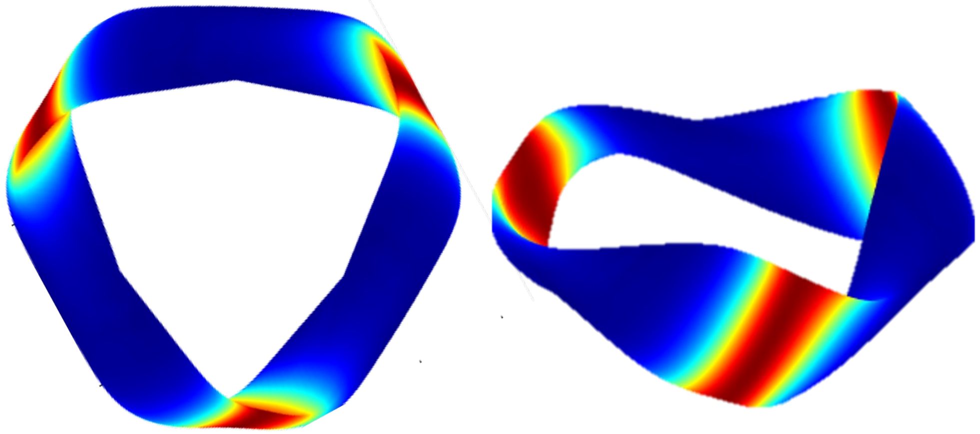

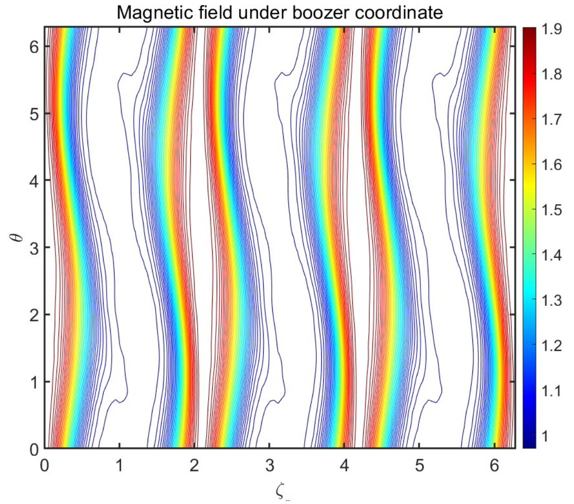

SQUID-like but lack of turbulence optimization

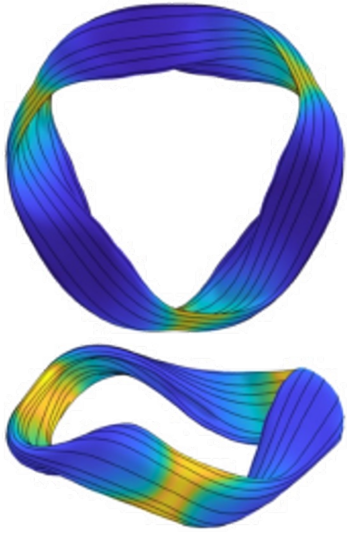

[Goodman 2024]

Omnigenity Example

Toroidal Omnigenity And Helical Omnigenity

TO Nfp = 2 Iota = 0.83-0.75 A=6 with WARMSTART

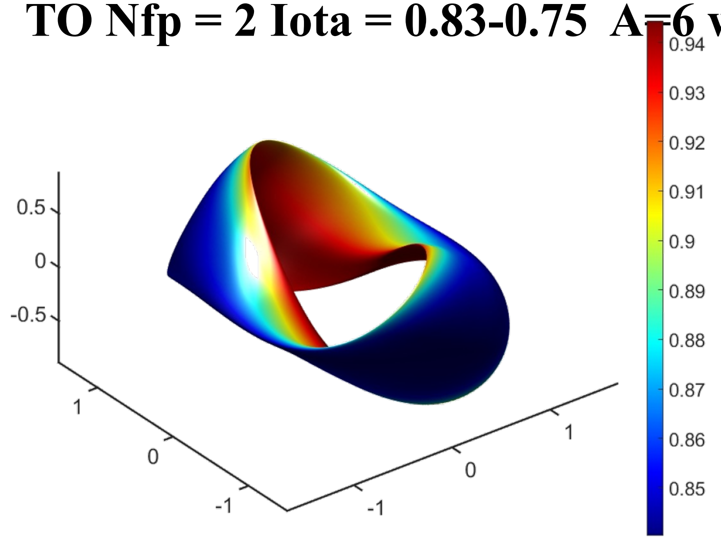

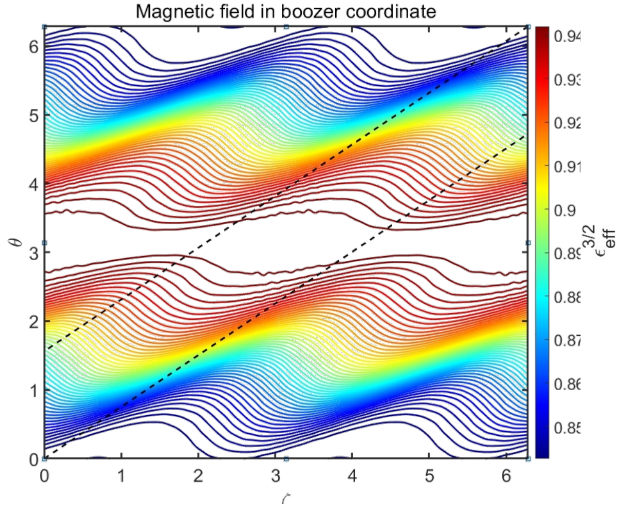

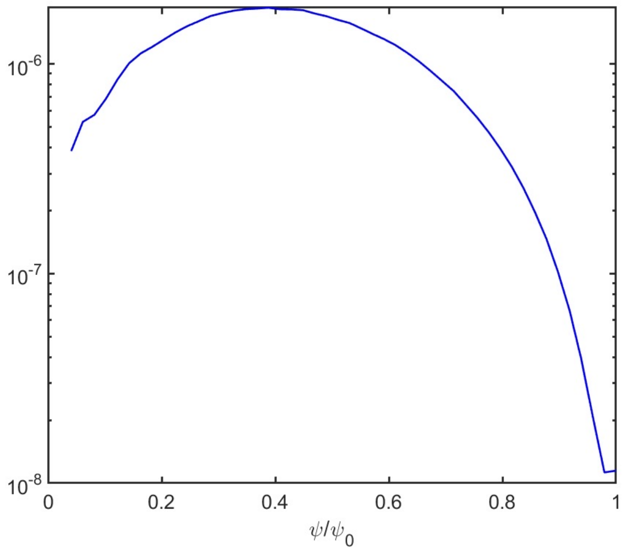

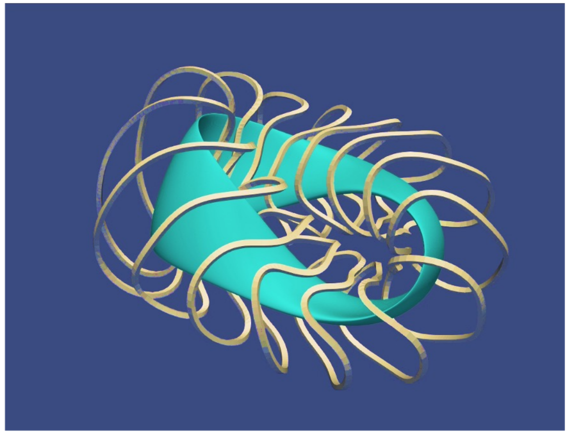

HO Nfp = 4 Iota = -1.23—1.34 A=8 with WARMSTART

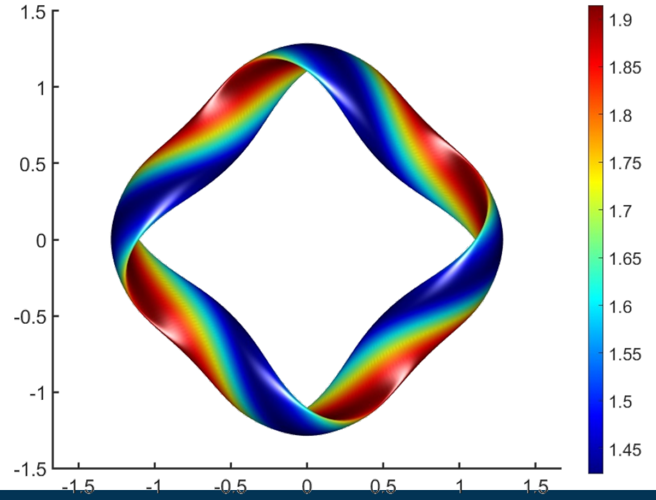

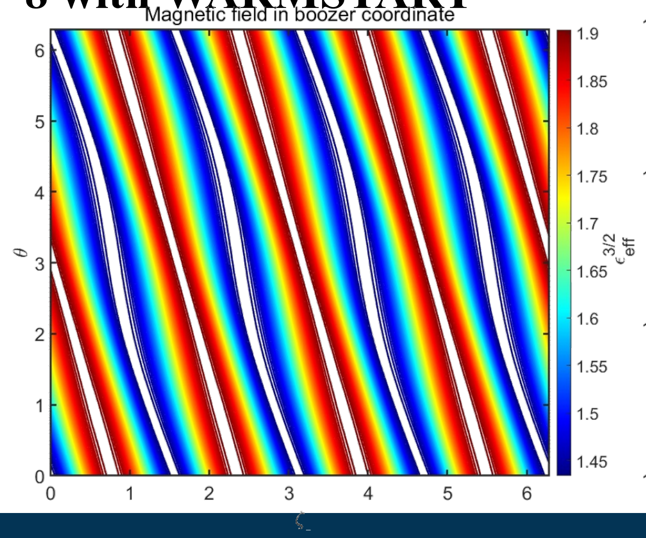

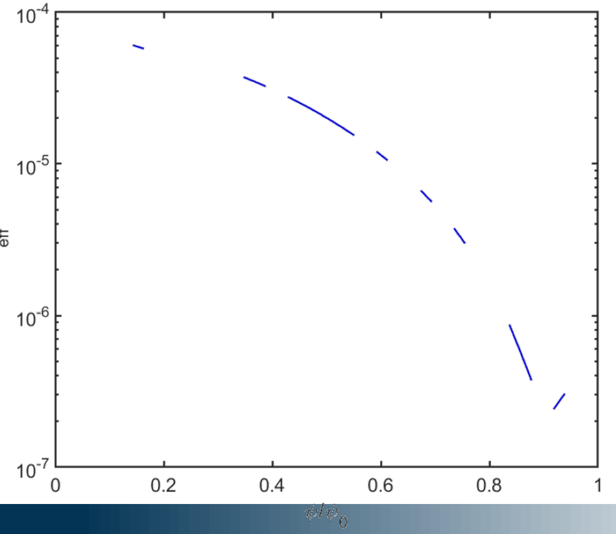

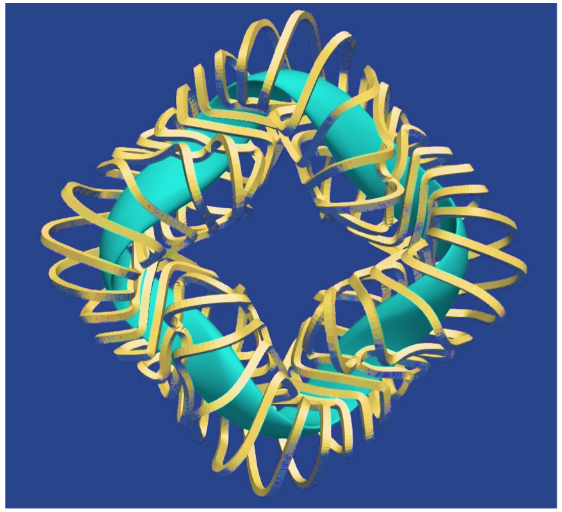

感谢您的关注！

Thank you for your attention!

The Magnetic Gradient Scale Length Explains Why Certain Plasmas Require Close External Magnetic Coils

By John Kappel, Matt Landreman, and Dhairya Malholtra

In Pre-print: arxiv.org/abs/2309.11342 (2023)

Stellarators Need Space for a Breeding Blanket & Neutron Shielding

During the design of ARIES-CS and W7-X, both configurations experienced engineering issues related to the space between the last closed flux surface and the external coils.[1][2]

This "plasma-coil separation" must be > 1.5m to have enough room for neutron shielding and a blanket.

Larger plasma-coil separation reduces coil ripple, accommodates for shifts during startup and initialization, and can allow larger configurations to be scaled down.

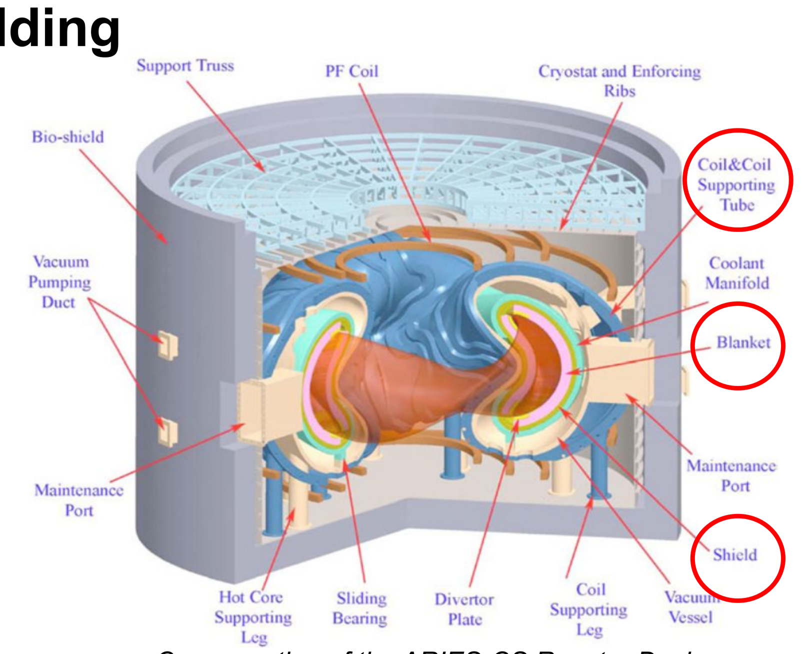

Cross-section of the ARIES-CS Reactor Design

Difficulty of Increasing Plasma-Coil Separation in Stage II Optimization

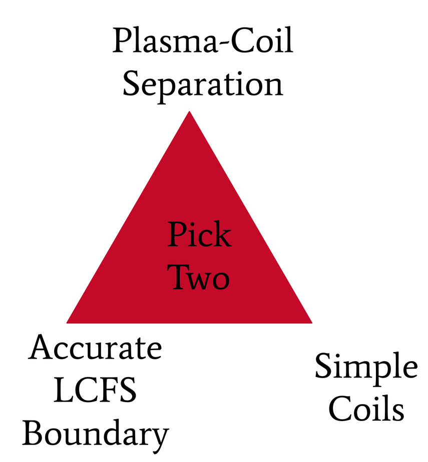

Moving coils further away from the plasma results in increased coil complexity (such as increased curvature, longer coils, and closer minimum coil-coil distance), as shown on the right.

Single-stage optimization[3] can be computationally challenging. **It is therefore valuable to develop an easy-to-calculate proxy for plasma-coil separation.**

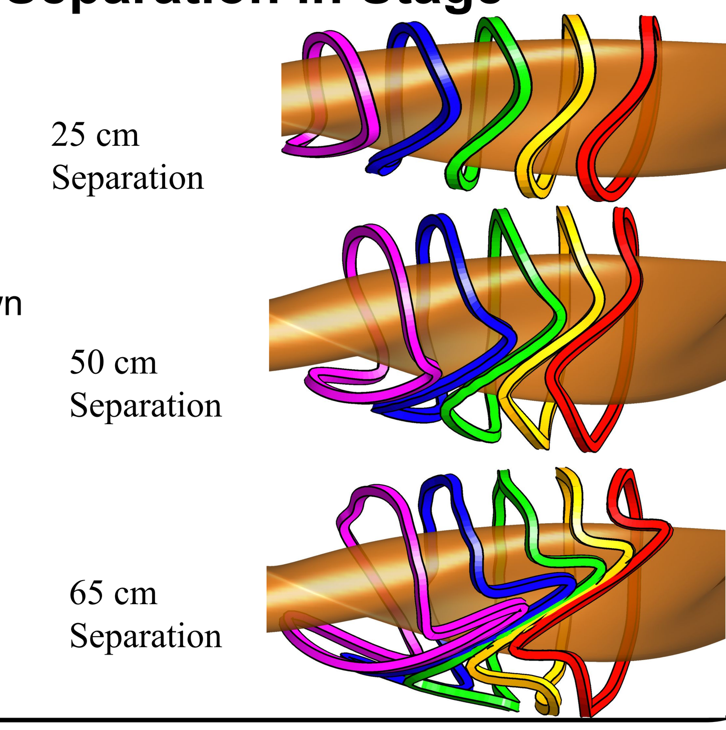

Intuition for Magnetic Gradient Scale Length

Arguments of scale lengths are used in plasma physics to determine which effects are negligible versus significant.

A spatial gradient of the magnetic field encodes some information about the spatial distance from the coils to the plasma.

$$\nabla\mathbf{B} = \begin{bmatrix} \frac{\partial B_x}{\partial x} & \frac{\partial B_y}{\partial x} & \frac{\partial B_z}{\partial x} \\ \frac{\partial B_x}{\partial y} & \frac{\partial B_y}{\partial y} & \frac{\partial B_z}{\partial y} \\ \frac{\partial B_x}{\partial z} & \frac{\partial B_y}{\partial z} & \frac{\partial B_z}{\partial z} \end{bmatrix}$$

$$\boxed{L_{\nabla\mathbf{B}} = \frac{\sqrt{2}B}{\|\nabla\mathbf{B}\|_F}} \qquad \|A\|_F = \sqrt{\sum_{i=1}^{m}\sum_{j=1}^{n}|a_{ij}|^2}$$

Model Geometry: Infinite Straight Wire

For a current carrying infinite straight wire, $L_{\nabla\mathbf{B}}$ is equal to the distance between the magnetic field and the wire. Therefore, by measuring the magnetic field and its gradient, we can determine where the nearest wire must be located to create the magnetic field.

$$\mathbf{B}(R) = \frac{\mu_0 I}{2\pi R}\hat{\boldsymbol{\phi}}$$

$$\nabla\mathbf{B} = -\frac{\mu_0 I}{2\pi R^2}(\hat{\boldsymbol{\phi}}\hat{\mathbf{R}} + \hat{\mathbf{R}}\hat{\boldsymbol{\phi}}),$$

$$\|\nabla\mathbf{B}\|_F = \frac{\sqrt{2}\mu_0 I}{2\pi R^2},$$

$$L_{\nabla\mathbf{B}} = \sqrt{2}\frac{B}{\|\nabla\mathbf{B}\|_F} = R.$$

Read Paper Here:

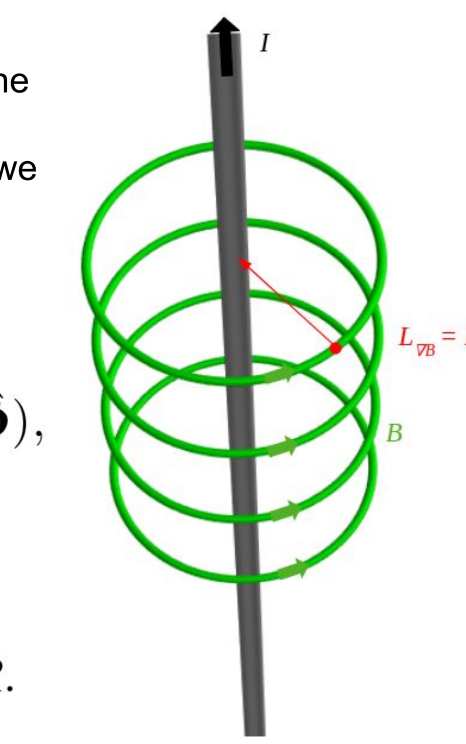

REGCOIL[4] is a Useful Optimizer to Systematically Compare the Coils of Many Configurations

`REGCOIL`'s objective function **preserves convexity**, so any local minimum is a global minimum. It also has fewer tuning parameters than other codes.

`REGCOIL` calculates the surface current density on a **winding surface**, which is outside the LCFS at a constant distance L. This is used to find the magnetic field of the plasma, as shown below:

$$\Phi'(\theta',\zeta') = \sum_j \Phi_j \sin(m_j\theta' - n_j\zeta')$$

$$\mathbf{K}' = \mathbf{n}' \times \nabla\Phi'$$

$$\mathbf{B}(\mathbf{r}) = \frac{\mu_0}{4\pi}\int d^2a' \frac{\mathbf{K}' \times (\mathbf{r}-\mathbf{r}')}{|r-r'|^3}$$

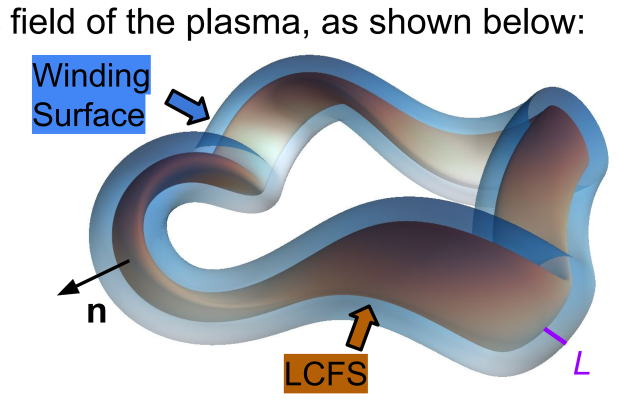

REGCOIL minimizes the following objective:

$$\boxed{f = \int d^2a\,(\mathbf{B}(\theta,\zeta)\cdot\mathbf{n})^2 + \lambda\int d^2a'\,\|\mathbf{K}(\theta',\zeta')\|^2}$$

2 free parameters: L and λ. A unique solution requires 2 constraints:

1. $B_{RMS} = B^*_{RMS}$
2. $\|K\|_\infty = \|K\|^*_\infty$

$$B_{RMS} = \left(\frac{\int d^2a\,(\mathbf{B}\cdot\mathbf{n})^2}{A_{Plasma}}\right)^{1/2}$$ $\mathbf{B_{RMS}}$ is a measure of accuracy in the LCFS, and changes with λ

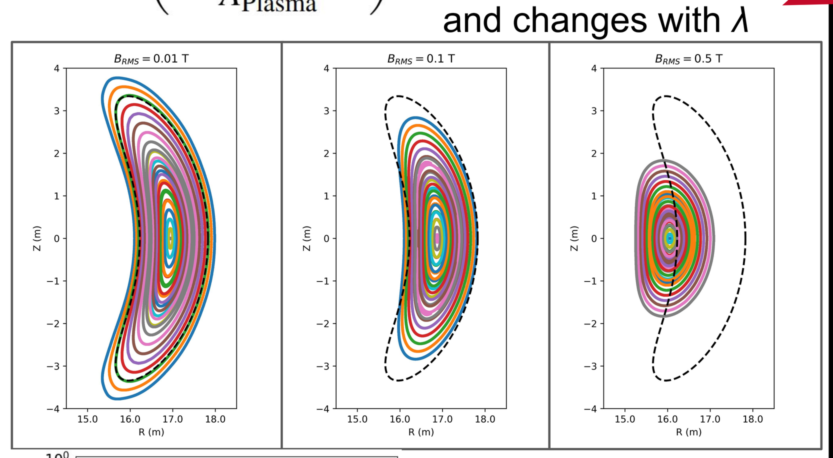

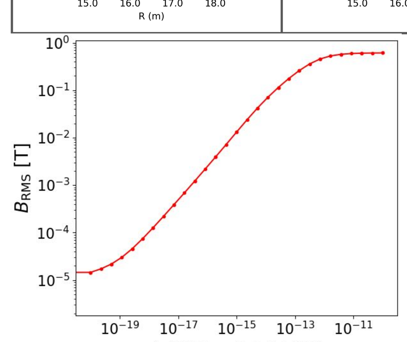

Ideally, B_{RMS} = 0, but the penalty for complex coils prevents this from being possible.

$\|K\|_\infty$ **or** K_{max} is the highest current density on the winding surface and uniquely defines plasma-coil separation.

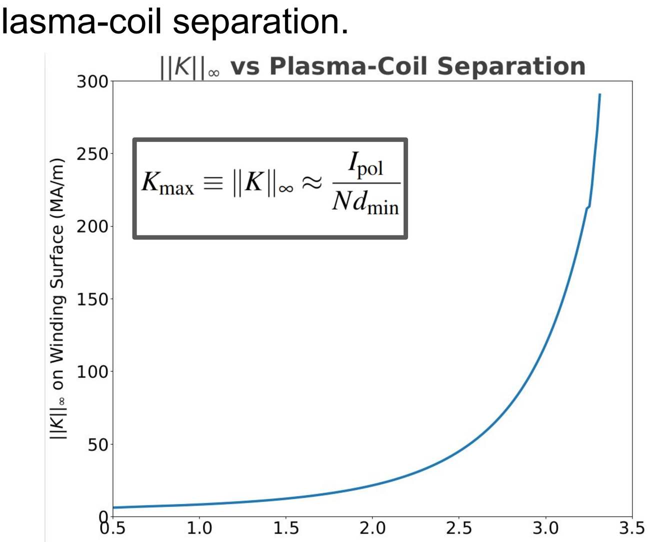

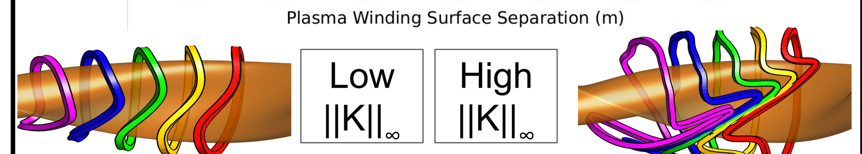

Virtual Casing Decomposes B_{coils} From B_{total}

Using virtual casing, it is possible to find the magnetic field generated by only the external coils, as shown below. We utilized work by Dhairya Malhotra[5][6] to perform virtual casing when $\beta > 0$.

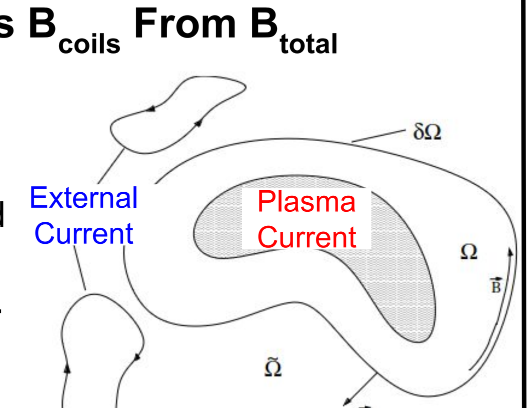

$$\mathbf{B}(\mathbf{x}) = \mathbf{B}_{plasma}(\mathbf{x}) + \mathbf{B}_{coils}(\mathbf{x})$$

$$\mathbf{B}^*_{coils}(\mathbf{x}) = -\frac{1}{4\pi}\oint_{\delta\Omega} d^2a\,\frac{(\mathbf{n}\times\mathbf{B}^*(\mathbf{p}))\times(\mathbf{x}-\mathbf{p})}{|x-p|^3}$$

Summary of REGCOIL Method

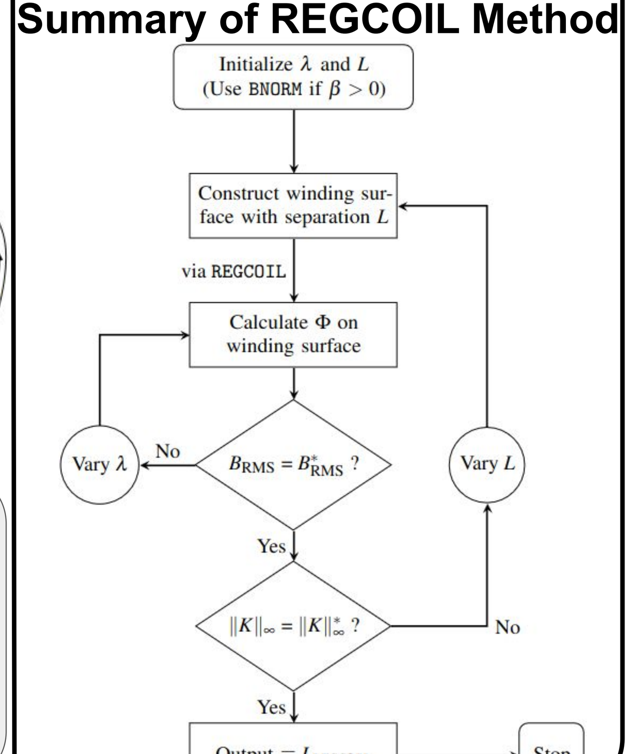

References

1. F. Najmabadi et al., *Fusion Science and Technology* **54**, 655–672 (2008)
2. T. Klinger et al., *Nuclear Fusion* **12**, 599 (1972).
3. R. Jorge, A. Goodman, M. Landreman, J. Rodrigues, and F. Wechsung, *PPCF* **65**, 074003 (2023).
4. M. Landreman, *Nuclear Fusion* **57**, 046003 (2017).
5. D. Malhotra, A. J. Cerfon, M. O'Neil, and E. Toler, *PPCF* **62**, 024004 (2019).
6. D. Malhotra, "Boundary integral equation solver for taylor states", github.com/hiddenSymmetries/virtual-casing (2019).

$L^*_{\nabla\mathbf{B}}$ Accurately Predicts Coil-Plasma Separation Found in Regcoil

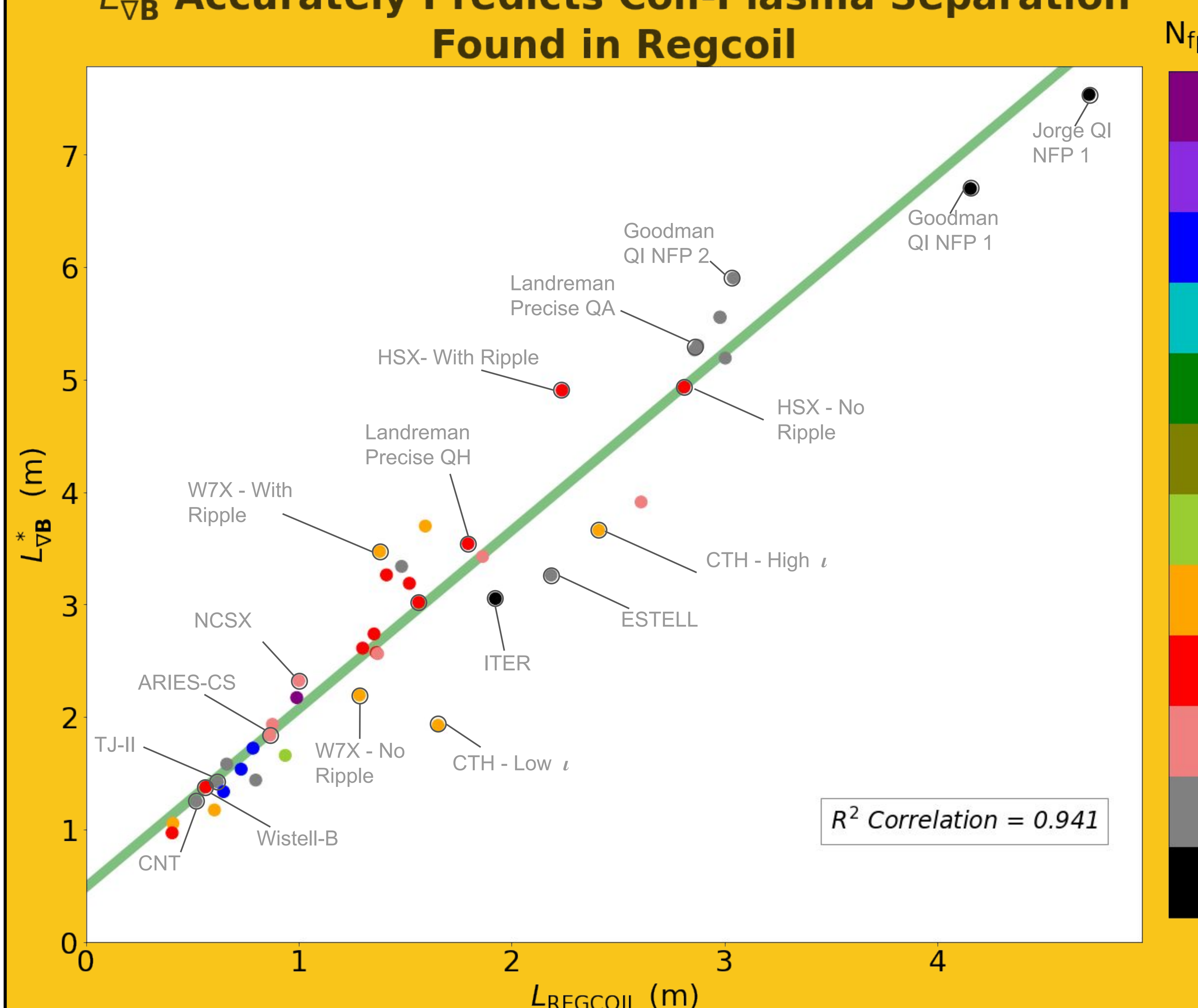

Parameters	$\|K\|^*_\infty$ = 17.16 MA/m	B_{Vol} = 5.865 T	m_θ & n_ζ = 96
B^*_{RMS} = 0.01 T	a = 1.704 m	mpol & ntor = 20	

We gathered database of > 40 stellarator and tokamak configurations. Within this database, the coil-to-plasma distance compared to the minor radius varies by over an order of magnitude. **The magnetic scale length** is well correlated to **the coil-to-plasma distance** of actual coil designs generated using the `REGCOIL` method.[4]

Below, we have plotted alternative scale lengths, which are also correlated with the coil-to-plasma distance.

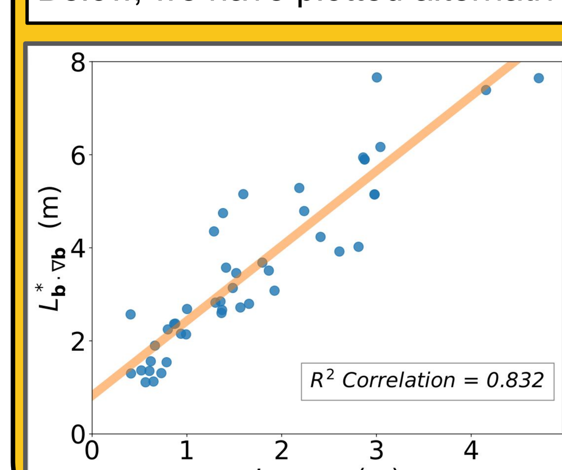

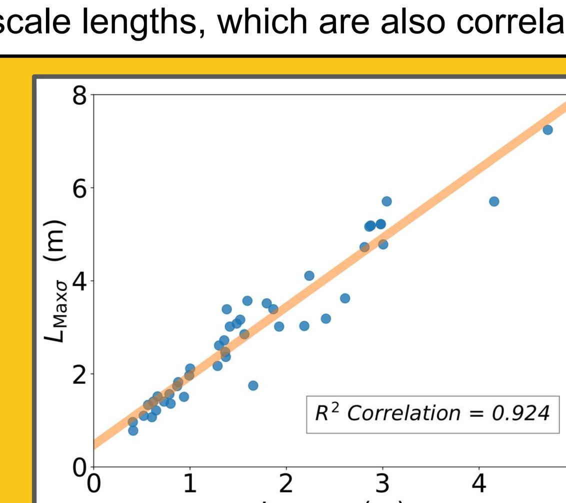

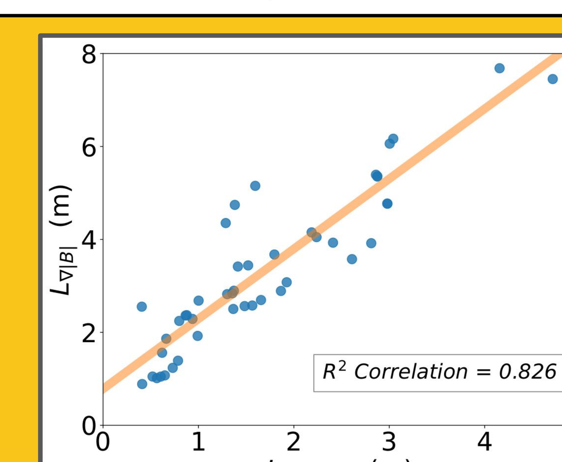

Discussion of Results

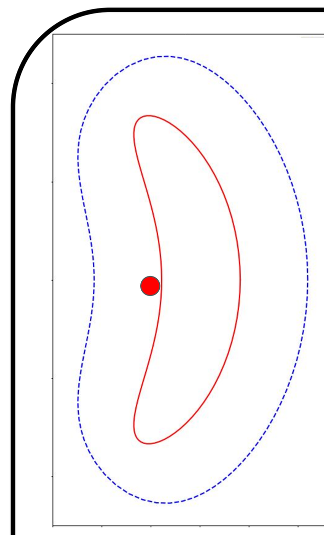

To the right is a NFP=4 QH stellarator on which $L_{\nabla\mathbf{B}}$ is plotted. It is shortest on the inside of the curve, or the "bean cross-section" shown on the left.

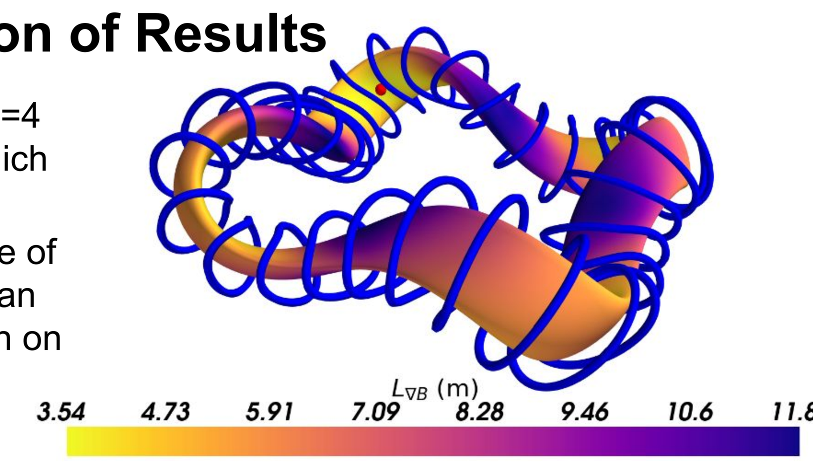

To the right, alternative scale lengths are shown on the surface of the NFP=4 QH stellarator. $L_{\nabla\mathbf{B}}$ matches $L_{\|\sigma\|}$ and is approximately equal to $L_{Max\sigma}$.

$$L_{\mathbf{b}\cdot\nabla\mathbf{b}} = \frac{1}{\|\mathbf{b}\cdot\nabla\mathbf{b}\|},$$

$$L_{\nabla|B|} = \frac{B}{\|\nabla B\|},$$

$$L_{\|\sigma\|} = \frac{\sqrt{2}B}{(\Sigma_i\sigma_i^2)^{1/2}},$$

$$L_{Max\sigma} = \frac{B}{\mathrm{Max}[\sigma_i]},$$

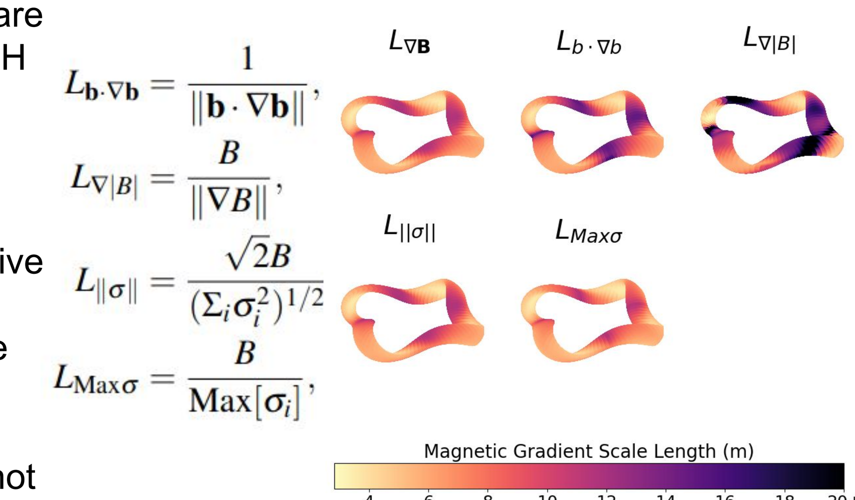

Results of the main figure are insensitive to target $\|K\|_\infty$ and B_{RMS} within a plausible range. Configurations that lie off the line of best-fit tend to be configurations with high coil-ripple, axisymmetric, or their VMEC files do not converge.

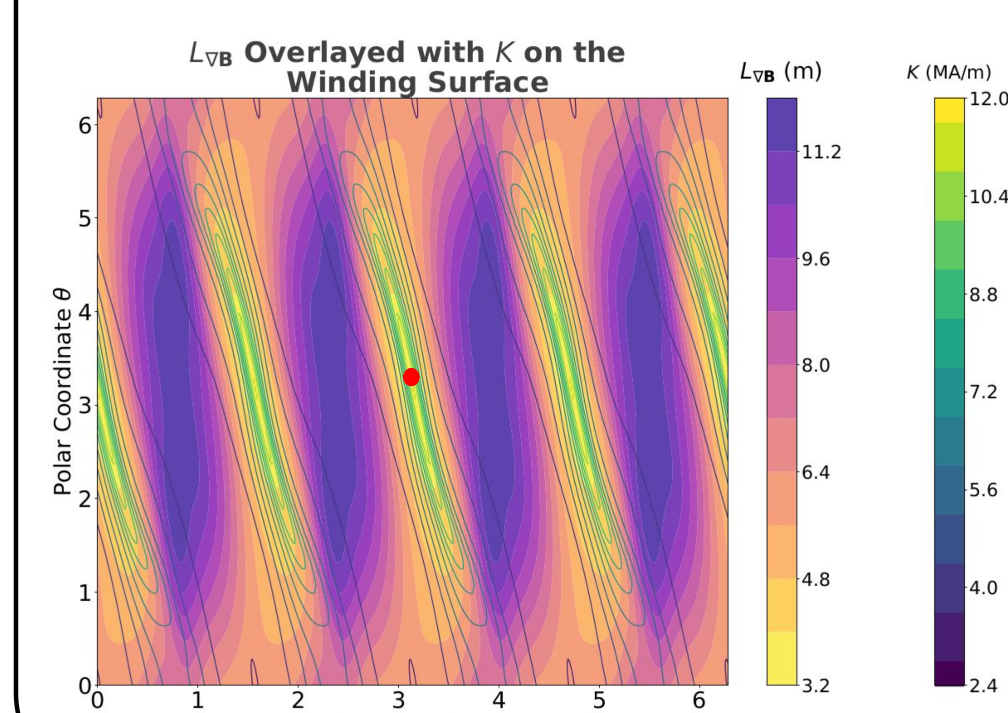

There is good spatial correlation between $\|K\|_\infty$ and $L^*_{\nabla\mathbf{B}}$. The smallest $L_{\nabla\mathbf{B}}$ and the largest $\|K\|_\infty$ are located in the same region.

Our future work is to implement $L^*_{\nabla\mathbf{B}}$ in the objective functions of Stage I optimizations (i.e., optimizing the plasma shape without explicitly considering the coil shapes).

This work was supported by the U.S. Department of Energy, Office of Science, Office of Fusion Energy Science, under award number DE-FG02-93ER54197. This research used resources of the National Energy Research Scientific Computing Center (NERSC), a U.S. Department of Energy Office of Science User Facility located at Lawrence Berkeley National Laboratory, operated under Contract No. DE-AC02-05CH11231 using NERSC award FES-ERCAP-mp217-2023.

MONKES: a fast neoclassical code for the evaluation of monoenergetic transport coefficients in stellarator plasmas

F. J. Escoto[1], J. L. Velasco[1], I. Calvo[1], M. Landreman[2] and F. I. Parra[3]

[1]Laboratorio Nacional de Fusión, CIEMAT, Madrid, Spain [2]University of Maryland, College Park, MD, USA [3]Princeton Plasma Physics Laboratory, Princeton, NJ, USA

Corresponding author: `fjavier.escoto@ciemat.es`

1. Neoclassical transport in stellarator optimization

- Stellarators can and must be neoclassically optimized in order to be fusion reactor candidates. Wendelstein 7-X has demonstrated that theoretically based optimization is effective [1].
- Radial transport has been addressed extensively in stellarator optimization. However, **direct optimization of the bootstrap current has not been tackled** so far.
- **Why has it been excluded?** An accurate calculation of the bootstrap current was too expensive to be included in optimization suites (except for configurations very close to quasi-symmetry [2]).

The new neoclassical code MONKES (MONoenergetic Kinetic Equation Solver) [3] can provide a **fast and accurate** evaluation of **all** the monoenergetic coefficients in stellarators.

2. Drift-kinetic equation (DKE) and transport coefficients

MONKES solves the same drift-kinetic equation as the code DKES [4]

$$\xi \boldsymbol{b}\cdot\nabla f_j + \frac{1}{2}\nabla\cdot\boldsymbol{b}(1-\xi^2)\frac{\partial f_j}{\partial \xi} - \frac{\widehat{E}_\psi}{\langle B^2\rangle}\boldsymbol{B}\times\nabla\psi\cdot\nabla f_j - \frac{\hat{\nu}}{2}\frac{\partial}{\partial\xi}\left((1-\xi^2)\frac{\partial f_j}{\partial \xi}\right) = s_j,$$

where $j\in\{1,2,3\}$, $\xi := \boldsymbol{v}\cdot\boldsymbol{b}/v$, $\hat{\nu} := \nu(v)/v$, $\widehat{E}_\psi := E_\psi/v$ and

$$s_1 := -\Omega_a \boldsymbol{v}_{\mathrm{m}a}\cdot\nabla\psi/Bv^2, \qquad s_2 := s_1, \qquad s_3 := \xi B/B_0.$$

With each solution, MONKES computes the monoenergetic geometric coefficients

$$\widehat{D}_{ij} := \left\langle \int_{-1}^{+1} s_i f_j \,\mathrm{d}\xi \right\rangle, \qquad i,j\in\{1,2,3\}.$$

For fixed $(\hat{\nu},\widehat{E}_\psi)$ the coefficients $\widehat{D}_{ij}$ depend only on the magnetic geometry. At most, only $\{\widehat{D}_{11},\widehat{D}_{13},\widehat{D}_{31},\widehat{D}_{33}\}$ are independent. Stellarator symmetry implies $\widehat{D}_{13} = -\widehat{D}_{31}$.

Monoenergetic coefficients allow to calculate neoclassical transport of species a as

$$\begin{bmatrix} \langle \boldsymbol{\Gamma}_a\cdot\nabla\psi\rangle \\ \langle \boldsymbol{Q}_a\cdot\nabla\psi\rangle/T_a \\ n_a\langle \boldsymbol{V}_a\cdot\boldsymbol{B}\rangle/B_0 \end{bmatrix} = \begin{bmatrix} L_{11a} & L_{12a} & L_{13a} \\ L_{21a} & L_{22a} & L_{23a} \\ L_{31a} & L_{32a} & L_{33a} \end{bmatrix} \begin{bmatrix} A_{1a} \\ A_{2a} \\ A_{3a} \end{bmatrix},$$

provided the thermodynamical forces

$$A_{1a}(\psi) := n_a'/n_a - 3T_a'/2T_a - e_a E_\psi/T_a,$$
$$A_{2a}(\psi) := T_a'/T_a$$
$$A_{3a}(\psi) := e_a B_0\langle \boldsymbol{E}\cdot\boldsymbol{B}\rangle/T_a\langle B^2\rangle.$$

The thermal transport coefficients L_{ij} can be obtained as integrals of the corresponding $\widehat{D}_{ij}$

$$L_{ija} := \int_0^\infty 2\pi v^2 f_{\mathrm{M}a} w_i w_j C_{ija}\widehat{D}_{ij}\,\mathrm{d}v\,,$$

where $w_1 = w_3 = 1$, $w_2 = v^2/v_{ta}^2$ and. For each species: $C_{ija} := -B^2v^3/\Omega_a^2$, $C_{i3a} := -Bv^2/\Omega_a$, $C_{3ja} := Bv^2/\Omega_a$ for $i,j\in\{1,2\}$ and $C_{33a} := v$.

3. Legendre expansion

The solution is represented as a truncated Legendre series

$$f = \sum_{k=0}^{N_\xi} f^{(k)} P_k(\xi).$$

In this basis the DKE has a **tridiagonal** structure

$$L_k f^{(k-1)} + D_k f^{(k)} + U_k f^{(k+1)} = s^{(k)},$$

for $k = 0,1,\ldots N_\xi$, where $f^{(-1)} := 0$.

The lower, diagonal and upper terms are spatial differential operators

$$L_k = \frac{k}{2k-1}\left(\boldsymbol{b}\cdot\nabla + \frac{k-1}{2}\boldsymbol{b}\cdot\nabla\ln B\right),$$

$$D_k = -\frac{\widehat{E}_\psi}{\langle B^2\rangle}\boldsymbol{B}\times\nabla\psi\cdot\nabla + \frac{k(k+1)}{2},$$

$$U_k = \frac{k+1}{2k+3}\left(\boldsymbol{b}\cdot\nabla - \frac{k+2}{2}\boldsymbol{b}\cdot\nabla\ln B\right).$$

4. Block tridiagonal algorithm

1. Forward elimination

Starting from $\Delta_{N_\xi} = D_{N_\xi}$ and $\sigma^{(N_\xi)} = s^{(N_\xi)}$ we obtain recursively

$$\Delta_k = D_k - U_k\Delta_{k+1}^{-1}L_{k+1},$$
$$\sigma^{(k)} = s^{(k)} - U_k\Delta_{k+1}^{-1}\sigma^{(k+1)}.$$

for $k = N_\xi - 1, N_\xi - 2, \ldots, 0$. Each Δ_k and $\sigma^{(k)}$ are obtained performing Gaussian elimination over

$$\left[\begin{array}{cc|c} D_k & U_k & s^{(k)} \\ L_{k+1} & \Delta_{k+1} & \sigma^{(k+1)} \end{array}\right]$$

to eliminate U_k.

The system is factorized in a **lower triangular** form

$$L_k f^{(k-1)} + \Delta_k f^{(k)} = \sigma^{(k)}.$$

2. Backward substitution

Once factorized, the system is easily solved

$$f^{(k)} = \Delta_k^{-1}\left(\sigma^{(k)} - L_k f^{(k-1)}\right),$$

for $k = 0,1,\ldots N_\xi$.

- Discretizing the flux-surface in N_{fs} points, L_k, D_k, U_k and Δ_k are approximated by $N_{\mathrm{fs}}\times N_{\mathrm{fs}}$ matrices.
- MONKES employs Boozer angles (θ,ζ) and a pseudospectral Fourier discretization with N_θ and N_ζ points ($N_{\mathrm{fs}} = N_\theta N_\zeta$).
- For calculating $\widehat{D}_{ij}$ only $\{f^{(k)}\}_{k=0}^{2}$ are needed. Memory required is minimal $\sim O(N_{\mathrm{fs}}^2)$ and typically fits in a single core.
- The solution requires inverting $N_\xi + 1$ matrices of size $N_{\mathrm{fs}} \sim O(N_{\mathrm{fs}}^3 N_\xi)$ operations.

5. Benchmark of monoenergetic coefficients

Benchmark for three different magnetic configurations and two values of $\widehat{E}_\psi$ corresponding to the $1/\nu$ and $\sqrt{\nu}-\nu$ regimes. All $\widehat{D}_{ij}$ are given in metres.

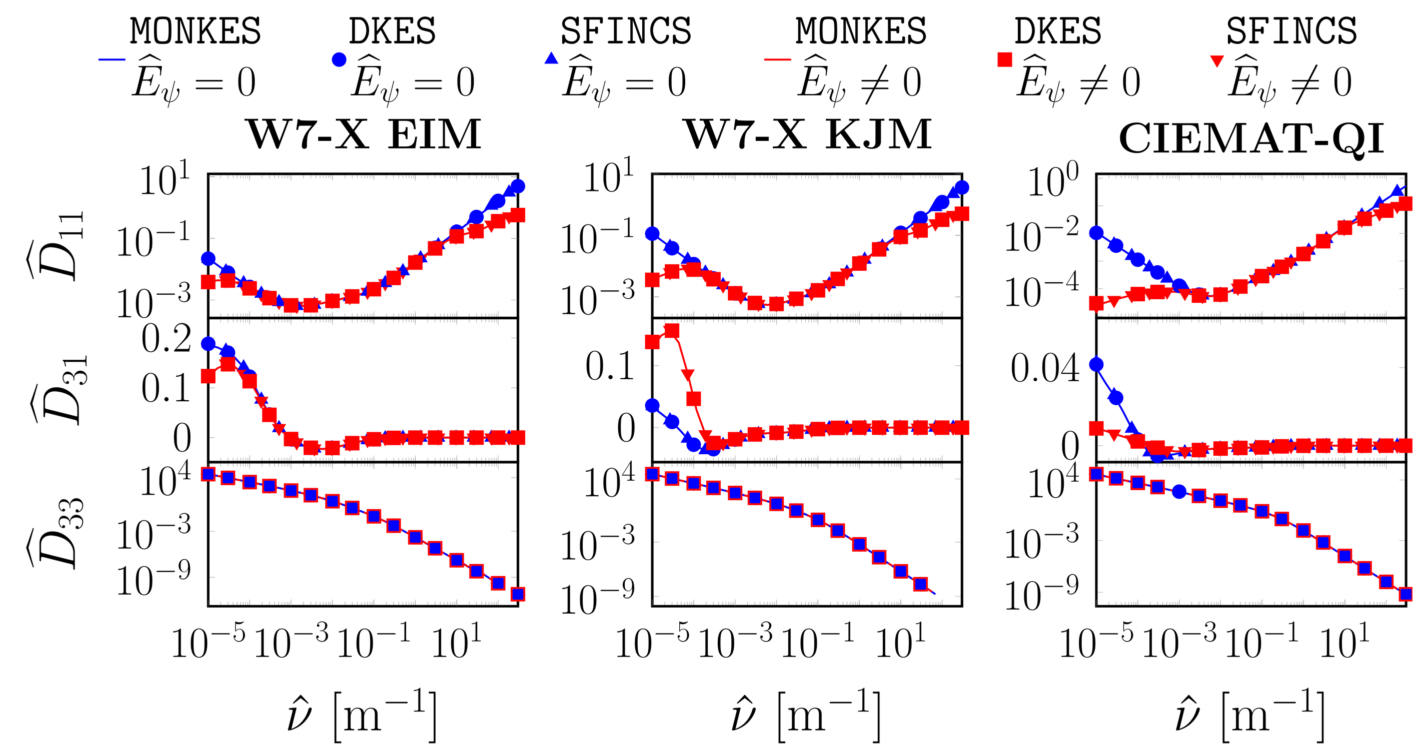

6. Code performance

Wall-clock times[a] of MONKES and DKES, using a single core, for the same level of relative convergence.

Case ($\hat{\nu} = 10^{-5}$ m^{-1})	$t_{\mathrm{clock}}^{\mathrm{DKES}}$	$t_{\mathrm{clock}}^{\mathrm{MONKES}}$
W7X-EIM $\widehat{E}_\psi = 0$	90 s	22 s
W7X-EIM $\widehat{E}_\psi \neq 0$	172 s	35 s
W7X-KJM $\widehat{E}_\psi = 0$	698 s	31 s
W7X-KJM $\widehat{E}_\psi \neq 0$	421 s	47 s
CIEMAT-QI $\widehat{E}_\psi = 0$	1060 s	76 s
CIEMAT-QI $\widehat{E}_\psi \neq 0$	4990 s	76 s

[a]All wall-clock times shown in what follows correspond to the cores of CIEMAT's cluster.

Arithmetical complexity $\sim C_{\mathrm{alg}} N_\xi N_{\mathrm{fs}}^3$. Verification with MONKES wall-clock time.

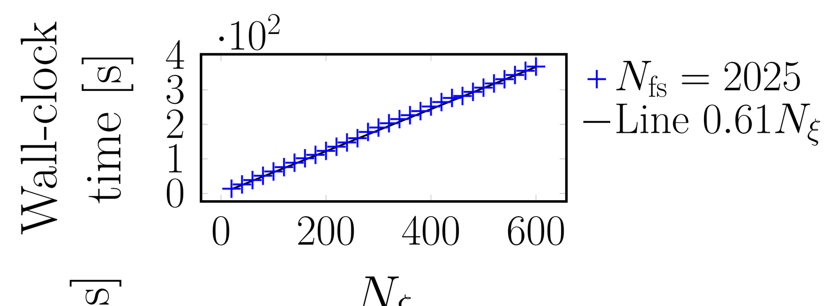

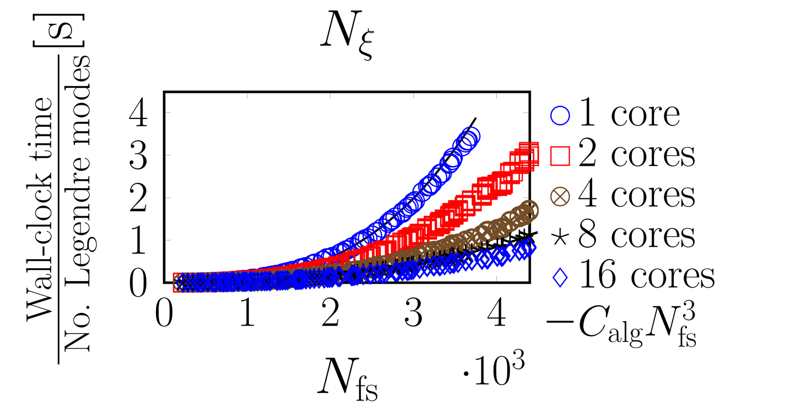

MONKES is much faster than DKES. Its algorithm scales linearly with N_ξ and cubicly with N_{fs}. For $N_{\mathrm{fs}} \leq 2000$ and $N_\xi \leq 200$, rapid calculations (≤ 2 minutes) on a single core. Can run even faster using more cores.

7. Exploring piecewise omnigenity

In a piecewise omnigenous magnetic field (pwO) [5], the second adiabatic invariant $J := \oint v_\| \,\mathrm{d}l$ is a flux-function only **piecewisely**.

A simple pwO field can be modelled as

$$B(\theta,\zeta) = B_{\min} + (B_{\max} - B_{\min}) \times \exp\left(-\left(\frac{\zeta}{w_\zeta}\right)^{2p} - \left(\frac{\theta - t_\zeta\zeta}{w_\theta}\right)^{2p}\right),$$

in the limit $p\to\infty$ along with a constraint to the rotational transform

$$\iota = -t_\zeta \frac{N_{\mathrm{fp}} w_\zeta}{\pi - N_{\mathrm{fp}} w_\zeta}.$$

Isolines of B for $p = 10$

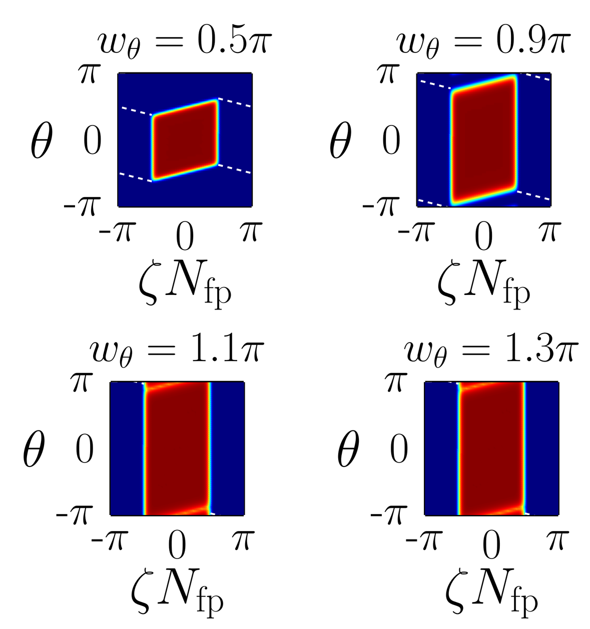

MONKES has been used to identify regions of the parameter space (p, w_θ) of pwO magnetic fields with small $\widehat{D}_{11}$ and $|\widehat{D}_{31}|$.

Both $\widehat{D}_{11}$ and $\widehat{D}_{31}$ are given in non-dimensional units.

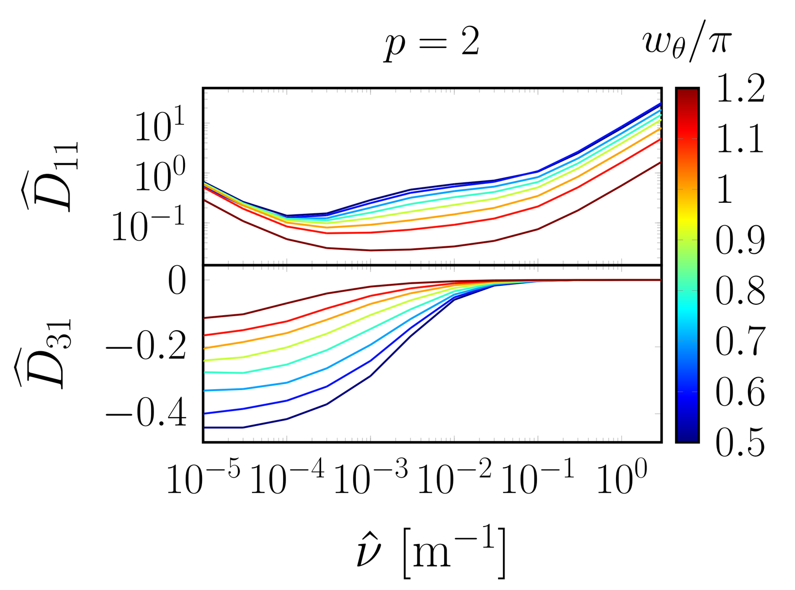

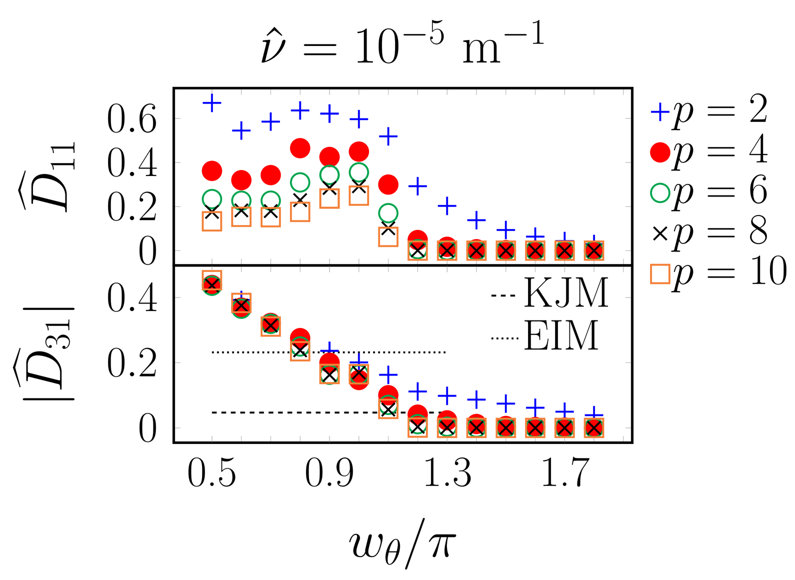

8. Ongoing work and future plans

- Use MONKES for direct optimization of the bootstrap current in stellarators.
- Include MONKES in predictive transport frameworks.
- Extend MONKES for multispecies momentum-conserving calculations.

[1] C. D. Beidler et al. *Nature* 596.7871 (2021).
[2] M. Landreman et al. *Physics of Plasmas* 29.8 (2022).
[3] F. J. Escoto et al. *Nuclear Fusion* 64.7 (2024).
[4] S. P. Hirshman et al. *The Physics of Fluids* 29.9 (1986).
[5] J. L. Velasco et al. *arXiv:2405.07634*. (2024).

MONKES paper MONKES GitHub

GOBIERNO DE ESPAÑA MINISTERIO DE CIENCIA, INNOVACIÓN Y UNIVERSIDADES Ciemat Centro de Investigaciones Energéticas, Medioambientales y Tecnológicas
Laboratorio Nacional de Fusión Ciemat
UNIVERSITY OF MARYLAND
PPPL PRINCETON PLASMA PHYSICS LABORATORY
EUROfusion
This work has been carried out within the framework of the EUROfusion Consortium, funded by the European Union via the Euratom Research and Training Programme (Grant Agreement No 101052200 — EUROfusion). Views and opinions expressed are however those of the author(s) only and do not necessarily reflect those of the European Union or the European Commission. Neither the European Union nor the European Commission can be held responsible for them.

EM analysis workflow for SPARC tokamak
Bring-up of TF coil voltage tap signal conditioners

Sophia Arnold[1], Adam Kuang, Aria Lorenz, Paul Willis

Commonwealth Fusion Systems (CFS), a world leader in the fusion energy industry, are set to make history with their proof-of-principle SPARC tokamak as the world's first commercially relevant, Q>1 fusion system.

EM analysis workflow for the SPARC tokamak

The Biot-Savart Law

$$\vec{B} = \frac{\mu_0 I}{4\pi} \int \frac{d\vec{s} \times \hat{r}}{r^2}$$

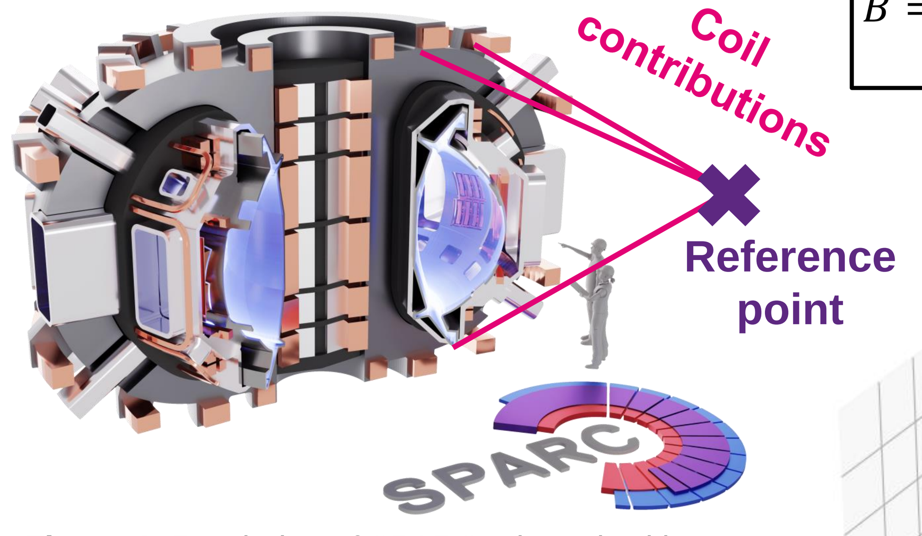

Figure 1. Rendering of SPARC tokamak with visual of magnetic field contributions on a position outside of system.

This package uses the **Biot-Savart law** to calculate the magnetic fields induced by SPARC at specified reference points outside of the tokamak. To use this law, the package estimates each individual **path integral** by **utilizing numerical integration techniques.**

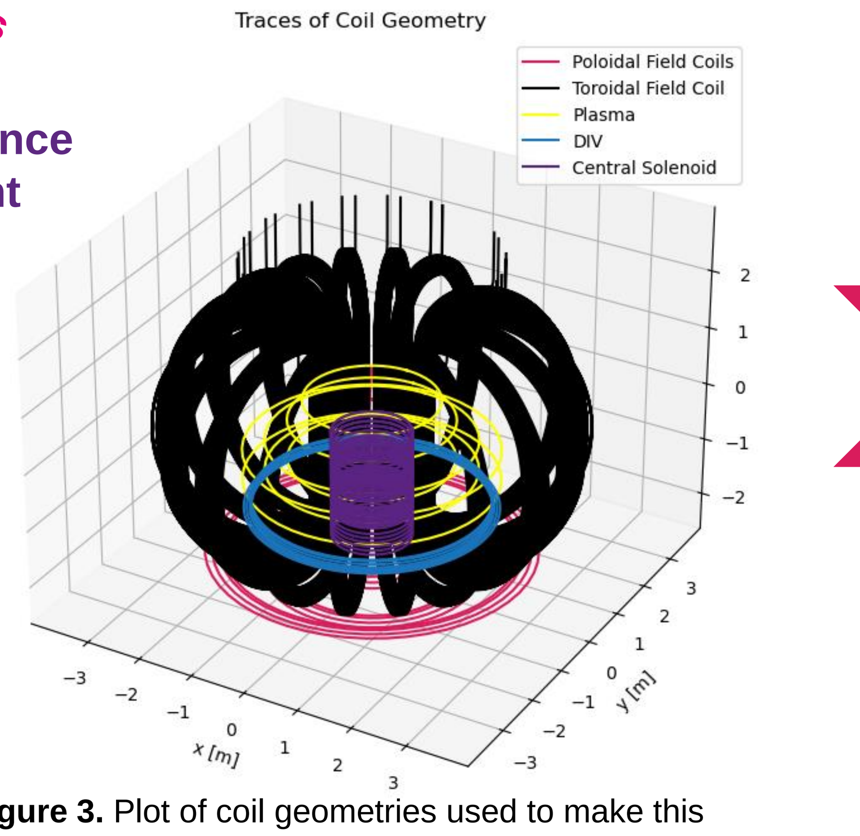

Figure 3. Plot of coil geometries used to make this Biot-Savart calculation within workflow. Only lower CS and PF coils plotted for better visibility, and selected plasma traces.

The workflow in use

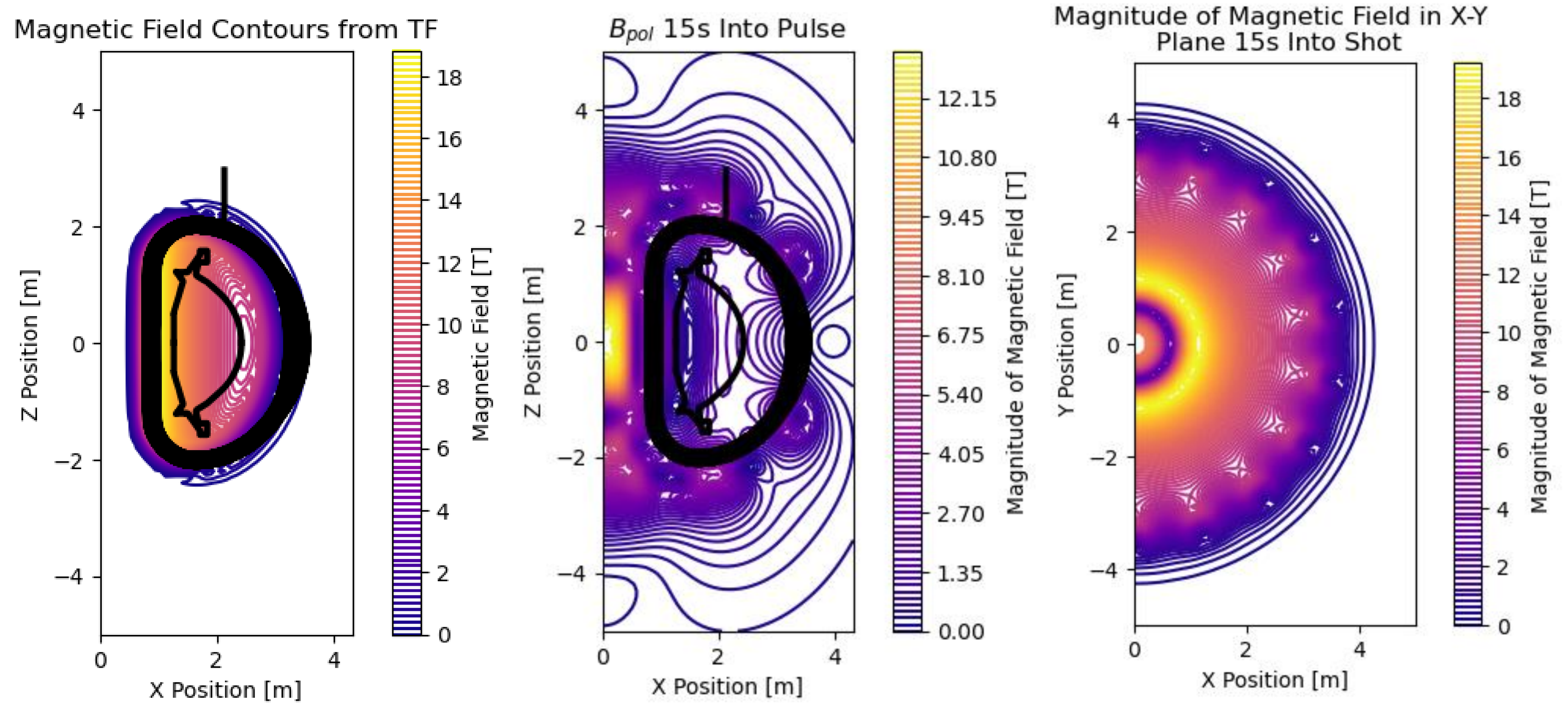

Figure 4, 5, 6. Output plots from EM analysis package.

Purpose

Prior to my arrival, at CFS there were multiple codes available to calculate the magnetic fields caused by SPARC. The goal of this project was to **centralize a workflow** for **3D magnetic field** calculations and **version control the coil geometries** being used. The other standard tool for magnetic field calculations is done through ANSYS and is the primary workflow for detailed design and high-fidelity predictions. However, this workflow **is computationally slow**, especially when evaluating locations further from the tokamak.

High-level pipeline diagram

Figure 2. High-level pipeline diagram for field-solver package.

This field solver workflow was designed for **wide-spread deployment across groups at CFS**, acting as the **source of truth for all future field-solvers**. As realistic uses for this package range from predictions on **induced EMF** on the instruments **by the changing magnetic fields** to estimating **overturning moments due to eddy currents on conducting structures**, the package needed to **offer varying degrees of fidelity**. To do this, I built this workflow in stages, each with its own optionality. Specifically, the workflow begins by reading coil geometries. Then, it moves into calculating the magnetic field per current at a series of reference points. And lastly, it multiplies the coil currents through the values.

As this workflow was designed to be **faster** and more **generalized** than the standard ANSYS one, conducting structures were not included in the model. This workflow is a **slight overestimation** of the rate of change of the fields induced by the tokamak, but when solving the engineering problems reliant on these calculations, an **overestimation** is **necessary**.

Conclusions

This EM analysis workflow has already shown its **utility** for many groups within CFS. As this workflow was designed to be **user-friendly**, it has and will expand the number of people who are **independently able to calculate the magnetic field induced by SPARC**. This workflow allows engineers and physicists at CFS alike to get a realistic assessment of the magnetic fields surrounding the tokamak, without **wasting** time and computational power running a model that is more detailed than necessary for many calculations.

To reiterate, this workflow is a great tool for getting an estimate of magnetic field strength induced by the SPARC tokamak. This is an **updateable**, **adaptable** package with widespread uses throughout different groups within Commonwealth Fusion Systems.

Toroidal field magnet voltage tap signal conditioner bring-up

Purpose

The operation of SPARC requires both **rapid, accurate quench prevention technology** for preservation of the superconducting magnets and **high precision measurement** devices for determining the performance of coils and understanding the **real-time environment** both within and external to the tokamak. One device which will help CFS to reach the required measurement capabilities are voltage tap signal conditioners, which clean outputted voltage tap signals. My second project this summer was to perform the **bring-up and qualification testing of these boards.**

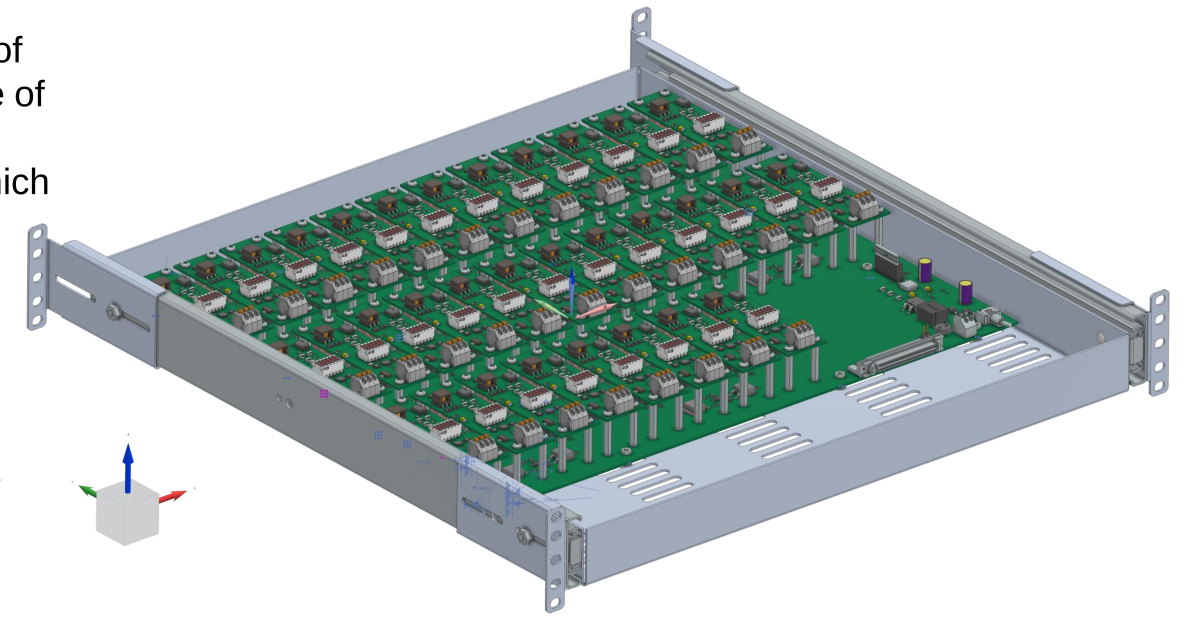

Figure 7. NX rendering TF coil voltage tap signal conditioner board. Intended use includes testing out of tokamak and within the tokamak hall during entire SPARC campaign.

Performance specifications

For these signal conditioners to meet the desired performance, they had to be designed with **particular specifications** in mind. Further, in the bring-up and qualification testing of these boards, I needed to prove whether the boards are hitting the desired specifications.

Some performance specifications include:

- High bandwidth
- ~µV noise floor
- High CMRR
- Avoidance of sequential logic machines

Some challenges we faced

Prior to starting the qualification testing and real bring-up, we needed to solve some issues that were **plaguing the performance of the boards**. Specifically, upon start-up, there was a **voltage railing behavior** that had not been there in previous iterations of the boards, that destroyed the output signal.

Solving this performance issue took up much of the initial weeks with the boards, as much trial and error was needed to find the fix.

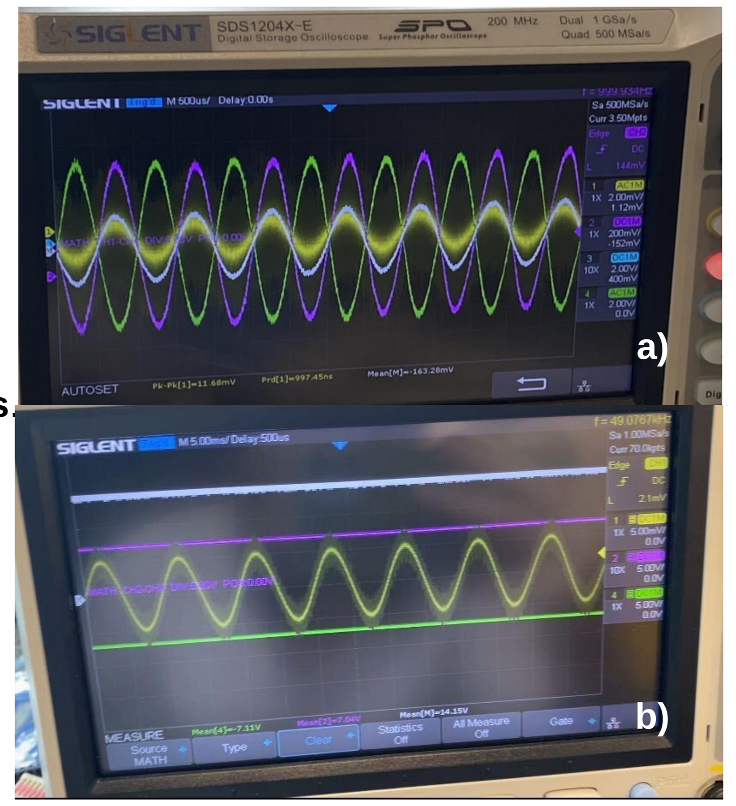

Figure 8.
a): Oscilloscope reading of successful test of of voltage tap signal conditioner.
b): Oscilloscope reading of unsuccessful test of voltage tap signal conditioner.

Conclusions

These **voltage tap signal conditioners** have already shown their worth as **accurate, reliable** signal conditioners for use within **TF coil testing** and in eventual **deployment within the tokamak basement**. Interesting technical challenges plagued the start of their bring-up, but now they have been showing their promise through the rounds of qualification testing.

Primary bring-up and qualification testing goals

- **Debugging stage – still developing these boards for large-scale use.**
- AC Qualification testing
- DC Qualification testing
- Bandwidth testing

Results from selected qualification tests

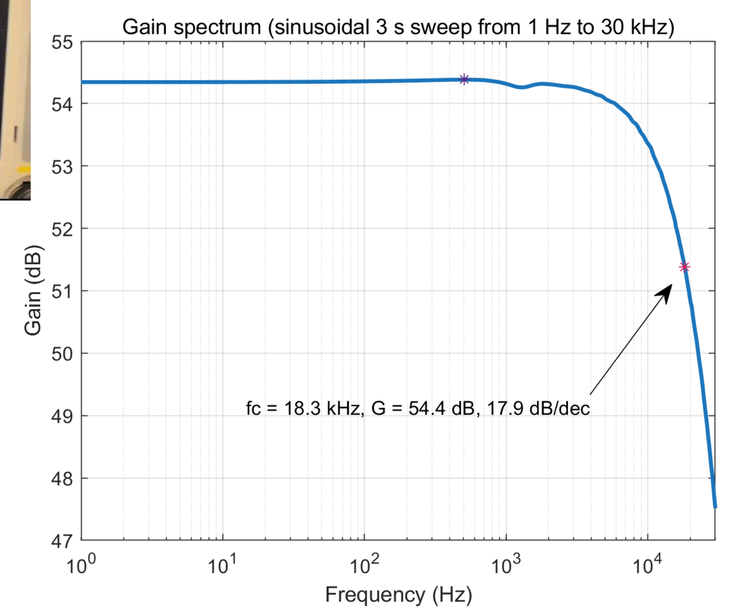

Figure 9. Gain spectrum from bandwidth testing on 16kHz interface board from 1k gain setting.

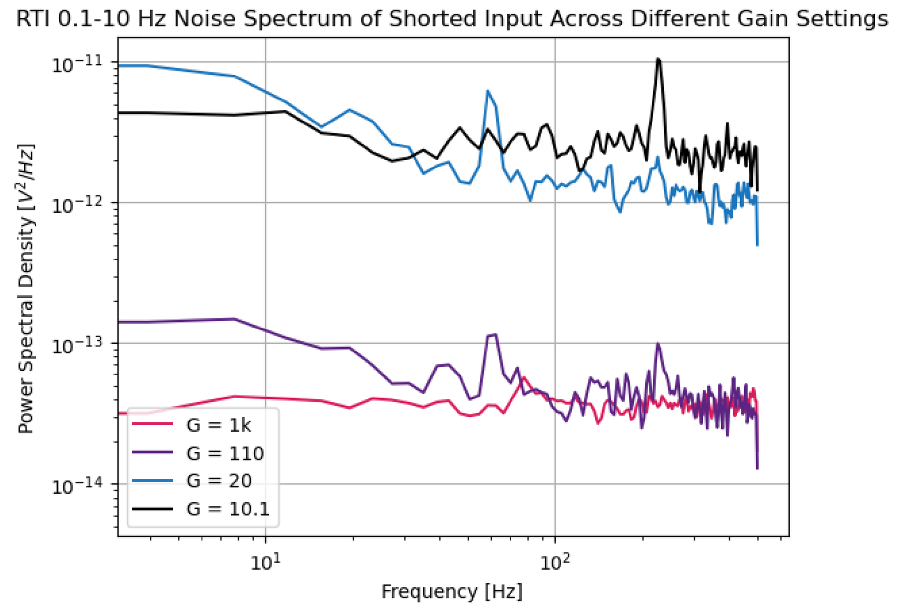

Figure 10. Noise floor analysis of various gain settings on 16kHz variant.

[1]sarnold@cfs.energy

mhdinn: Compact physics-informed neural network representations for 3D MHD equilibria

Timo Thun[1]*, Daniel Böckenhoff[1], Andrea Merlo[1], presented by Issra Ali[1]
[1]Max-Planck-Institut für Plasmaphysik

Wendelstein 7-X
MAX-PLANCK-INSTITUT FÜR PLASMAPHYSIK

INTRODUCTION

Solution of the magnetohydrodynamic force equilibrium equation (1) is at the backbone of modern stellarator optimization and data analysis.

$$\mathbf{F} = \mathbf{J} \times \mathbf{B} - \nabla p = 0 \tag{1}$$

The most succcessful and commonly used algorithm to solve this problem is the Variational Moments Equilibirium Code (VMEC) [2]. VMEC employs a Fourier series representation of the mapping from the field in magnetic coordinates (ρ, θ, ϕ), which is completely specified by the pressure and iota profiles, to geometric coordinates (R, λ, Z). However, this method is prohibitively slow for applications that involve real-time inference, such as control or flight simulators, as well as data-intensive algorithms such as stellarator optimization. Moreover, the VMEC implementation of the Fourier series mapping is neither compact nor differentiable in the ρ coordinate [1], making it suboptimal for stellarator optimization.

Neural networks have been used before to directly model VMEC flux surface topologies for faster inference [3]; however, there were non-physical artifacts in computation of the second derivative $\mathbf{B}$. A potential solution is physics-informed learning, where the network is trained on the force residual (1) as opposed to simply matching data from VMEC.

PHYSICS-INFORMED FUNCTION LEARNING

Physics-informed neural networks (PINNs) convert the solution of PDEs into an optimization problem. A neural network is used as an ansatz. The weights of the neural network are trained via gradient descent, with a residual of the relevant PDE/functional as the loss function (i.e. target function). The loss function may also contain boundary conditions, data points, etc. After training, the neural network is a pseudo-analytical solution of the PDE. No data is required for training.

Example: solving the intial value problem for the heat equation:

$$\frac{\partial u}{\partial t} = k\nabla^2 u, u(\mathbf{x}, t_0) = g(\mathbf{x}) \tag{2}$$

with neural network ansatz N.

Approximation: $\hat{u}(\mathbf{x}, t) = g(\mathbf{x}) + t \cdot \mathrm{N}(\mathbf{x}, t; \xi)$

Loss function: $\mathcal{L} = \partial_t \hat{u} - k\nabla^2 \hat{u}$

Training: $\mathrm{N}(\mathbf{x}, t; \xi)_{n+1} = \mathrm{N}(\mathbf{x}, t; \xi)_n + \alpha \frac{\partial \mathrm{N}}{\partial \xi}$

mhdinn

We seek to find a representation with the following properties simultaneously:

- Compactness and differentiability
- Fast inference time
- Physical consistency up to the second derivative

To this end, we propose mhdinn, a physics-informed neural network-based equilibrium code that solves for Fourier coefficients of the VMEC representation. The basic architecture is depicted in **Figure 3**. We demonstrate that the code is capable of function learning MHD equilibria, i.e. learning $R_{m,n}, \lambda_{m,n}, Z_{m,n}$ Fourier coefficients as a continuous function of the radial coordinate ρ for a specific $\iota(\rho), p(\rho)$, and boundary Fourier coefficients :

Approximation:

$$\hat{\mathbf{X}}_{m,n} = (\hat{R}_{m,n}(\rho), \hat{\lambda}_{m,n}(\rho), \hat{Z}_{m,n}(\rho)) = \rho^m(\mathbf{X}_{b;m,n} + (1-\rho^2)\mathrm{N}_{m,n}(\rho)) \tag{3}$$

Loss function:

$$\mathcal{L} = \mathbf{F} = \mathbf{J} \times \mathbf{B} - \nabla p \tag{4}$$

The loss function is computed in geometric coordinates using the same expressions initially derived in [2].

METHODOLOGY AND SELECTED RESULTS

mhdinn has been validated on a D-shaped axisymmetric tokamak profile, the Solovev equilibrium problem, as well as several 3D W7-X equilibria. Selected results for a W7-X equilibrium are plotted in **Figures 2** and **3**, and details the implementation are provided below. Good agreement is shown between the solution computed with VMEC and mhdinn; the largest error is in prediction of the location of the magnetic axis (order of centimeters). It should be noted that a similar discrepancy is found when comparing solutions of VMEC with DESC, another MHD equilibrium solver that uses the force residual as a target function as opposed to the energy functional (as VMEC does), for the same equilibrium with similarly low mode numbers M and N. The neural network used to generate the plots below used only 2112 parameters, whereas the VMEC solution would require 23 166 Fourier coefficents for the same number of toroidal and poloidal modes at a reasonable spatial discretization—a reduction of more than 10x.

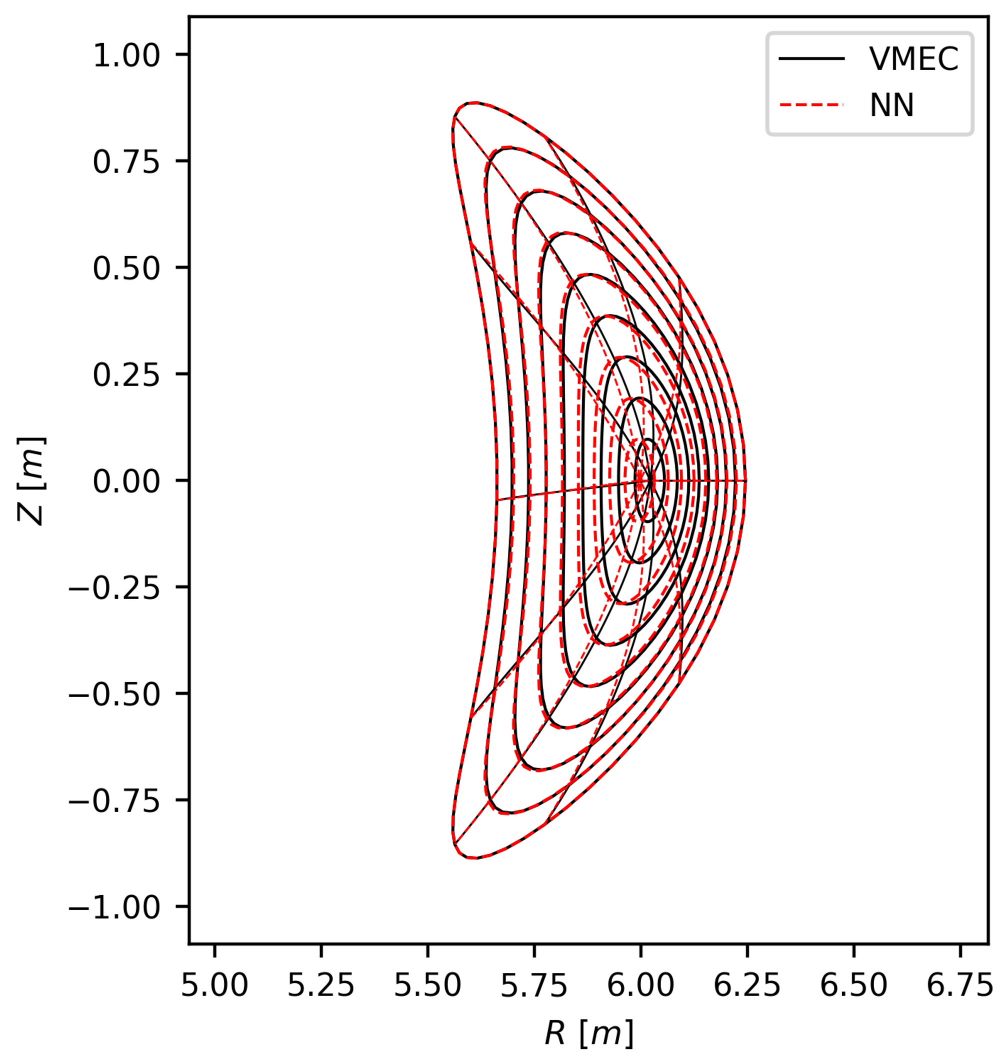

Figure 1: Comparison of VMEC Poincare plot and mhdinn Poincare plots, demonstrating the ability of mhdinn to replicate VMEC solutions with far less parameters (M, N = 6, 6)

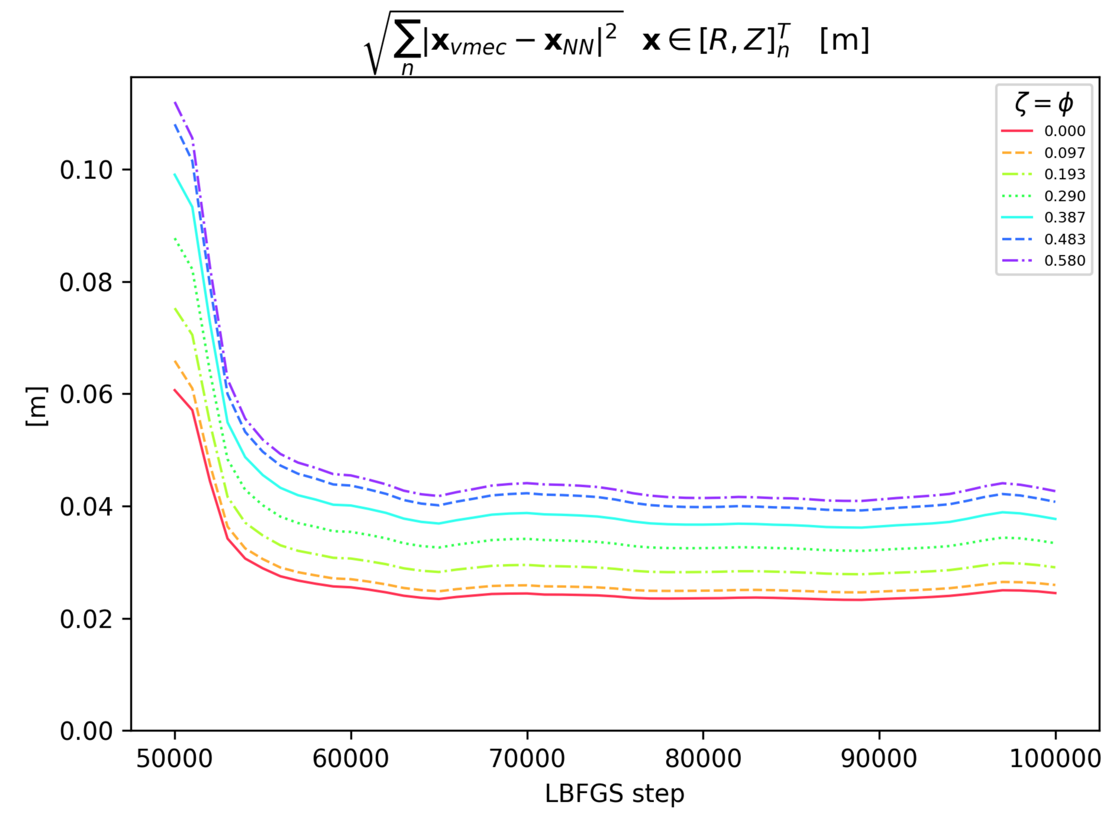

Figure 2: Mean squared error between mhdinn-computed and VMEC-computed magnetic axis positions (M, N = 6, 6)

mhdinn implementation

mhdinn has been implemented in python with the high performance JAX machine learning framework. It is packaged into a modular and easy-to-use command-line interface that offers flexibility in specifying model architecture, size, and training protocol.

The training process used 50 000 iterations of ADAM-W followed by 50 000 iterations of LBFG-S. The loss function was evaluated over a grid of 54 054 equidistant points in a W7-X half-field period. The neural networks used are simple multilayer perceptrons with two hidden layers of 16 parameters each.

SYSTEM ARCHITECTURE OF MHDINN

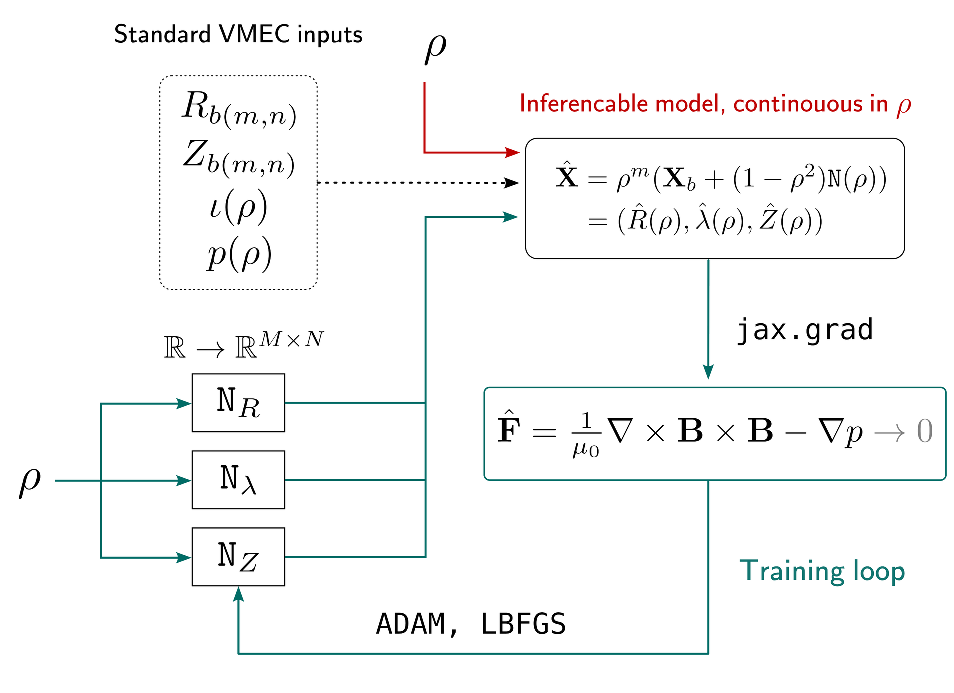

Figure 3: System architecture diagram of mhdinn, with training loop higlighted in blue and inference routine highlighted in red

KEY ADVANTAGES

Listed below are key advantages of mhdinn as MHD equilibrium representations over other methods.

- > 10x compression of VMEC MHD equilibria
- Precisely adjustable spectral density for R, λ, Z (impossible in VMEC)
- Differentiable and physically consistent up to the second derivative (as opposed to non-physics informed networks)

MILESTONES AND FUTURE WORK

☒ Function learning

Progress Training with force residual

Spin-offs Transfer learning, modified loss function, alternative representations to hard-code mathematical properties

☐ Operator learning

☐ Alternative models (e.g. MRxMHD)

☐ …

CONCLUSION

Physics-informed neural networks offer compact and quickly inferencable representations of MHD equilibria and are promising candidates for use in data or time-intensive applications, such as stellarator optimization or flight simulators. We have demonstrated their effectiveness in compressing solutions of the fixed-boundary VMEC problem over 10x. Next steps include finding network architectures that hard-code mathematical properties of the MHD solutions into the representations for more efficient learning and more compact representation, exploring more advanced problems such as MRxMHD, and working towards operator learning—training a neural network to learn a mapping from the VMEC input functions (i.e. $\iota(\rho), p(\rho), R_{b(m,n)}, Z_{b(m,n)}$) to a function that outputs Fourier coefficients as a function of ρ; i.e. a pseudoanalytical solution of the MHD boundary value problem over the entire configuration space of a fusion device.

[1] S.A. Henneberg, P. Helander, and M. Drevlak. "Representing the boundary of stellarator plasmas". In: *Journal of Plasma Physics* 87.5 (Sept. 2021). ISSN: 1469-7807. DOI: 10.1017/s0022377821000891. URL: http://dx.doi.org/10.1017/S0022377821000891.

[2] S. P. Hirshman and J. C. Whitson. "Steepest-descent moment method for three-dimensional magnetohydrodynamic equilibria". In: *The Physics of Fluids* 26.12 (Dec. 1983), pp. 3553–3568. ISSN: 0031-9171. DOI: 10.1063/1.864116. eprint: https://pubs.aip.org/aip/pfl/article-pdf/26/12/3553/12590952/3553_1_online.pdf. URL: https://doi.org/10.1063/1.864116.

[3] Andrea Merlo et al. "Proof of concept of a fast surrogate model of the VMEC code via neural networks in Wendelstein 7-X scenarios". In: *Nuclear Fusion* 61 (9 Sept. 2021), p. 096039. ISSN: 0029-5515. DOI: 10.1088/1741-4326/ac1a0d. URL: https://iopscience.iop.org/article/10.1088/1741-4326/ac1a0d.

Corresponding author: *timo.thun@ipp.mpg.de;
2024 Princeton Plasma Physics Laboratory / Simons Foundation Hidden Symmetries Graduate Summer School

EUROfusion

This work has been carried out within the framework of the EUROfusion Consortium, funded by the European Union via the Euratom Research and Training Programme (Grant Agreement No 101052200 — EUROfusion). Views and opinions expressed are however those of the author(s) only and do not necessarily reflect those of the European Union or the European Commission. Neither the European Union nor the European Commission can be held responsible for them.